

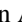
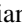


Mesoscale molecular assembly is favored by the active, crowded cytoplasm

Tong Shu ¹, Gaurav Mitra ², Jonathan Alberts, Matheus P. Viana,³ Emmanuel D. Levy,⁴
Glen M. Hocky ^{2,5,*} and Liam J. Holt ^{1,†}

¹*Institute for Systems Genetics, New York University Langone Medical Center, New York, New York 10016, USA*

²*Department of Chemistry, New York University, New York, New York 10003, USA*

³*Allen Institute for Cell Science, Seattle, Washington 98109, USA*

⁴*Department of Molecular and Cellular Biology, University of Geneva, 1211 Geneva 4, Switzerland*

⁵*Simons Center for Computational Physical Chemistry, New York University, New York, New York 10003, USA*



(Received 8 January 2024; accepted 5 June 2024; published 10 July 2024)

The mesoscale organization of molecules into membraneless biomolecular condensates is emerging as a key mechanism of rapid spatiotemporal control in cells. Principles of biomolecular condensation have been revealed through *in vitro* reconstitution. However, intracellular environments are much more complex than test-tube environments: they are viscoelastic, highly crowded at the mesoscale, and are far from thermodynamic equilibrium due to the constant action of energy-consuming processes. We developed synDrops, a synthetic phase separation system, to study how the cellular environment affects condensate formation. Three key features enable physical analysis: synDrops are inducible, bioorthogonal, and have well-defined geometry. This design allows kinetic analysis of synDrop assembly and facilitates computational simulation of the process. We compared experiments and simulations to determine that macromolecular crowding promotes condensate nucleation but inhibits droplet growth through coalescence. ATP-dependent cellular activities help overcome the frustration of growth. In particular, stirring of the cytoplasm by actomyosin dynamics is the dominant mechanism that potentiates droplet growth in the mammalian cytoplasm by reducing confinement and elasticity. Our results demonstrate that mesoscale molecular assembly is favored by the combined effects of crowding and active matter in the cytoplasm. These results move toward a better predictive understanding of condensate formation *in vivo*.

DOI: [10.1103/PRXLife.2.033001](https://doi.org/10.1103/PRXLife.2.033001)

I. INTRODUCTION

Cells are highly crowded, with macromolecules excluding 20–30% of cellular volume in eukaryotic cells and 30–40% in prokaryotic cells [1,2]. This high excluded volume can inhibit molecular motion, but on the other hand can entropically favor assembly through depletion attraction forces [3,4]. The majority of cytoplasmic volume is taken up by mesoscale (10 to 1000 nm diameter) particles [2]. This means that the effects of crowding strongly affect the behavior of mesoscale particles and assemblies, while having less impact on nanoscale processes because nanoscale particles can move relatively freely between mesoscale crowders, but mesoscale particles cannot. Studies have shown that macromolecular crowding can change biochemical reaction kinetics, protein conformations, and motor functions [4–6].

The cell also contains elastic networks that constrain and organize the cell interior. These include the actomyosin

cytoskeleton in the cytoplasm [7] and chromatin in the nucleus [8]. The presence of these networks and the high concentration of particles together make the intracellular environment viscoelastic. This contrasts with simple buffer solutions, which are only viscous.

Finally, cells are nonequilibrium open systems, and use adenosine triphosphate (ATP)-dependent cellular activities to maintain a nonequilibrium steady state by exchanging energy, information, and material with the extracellular environment, thereby locally reducing entropy [9]. Overall, the intracellular environment is highly complex, and its impact on the assembly of membraneless biomolecular condensates remains largely unexplored.

The assembly of membraneless biomolecular condensates bridges length scales between the nanoscale and mesoscale, where nanometer-sized molecules come together to form higher-order structures of tens to thousands of nanometers in diameter [10]. This wide range of length scales and timescales makes it difficult to predict how the crowded, active cellular environment will affect biomolecular condensate formation. Several studies have focused on the impact of elastic mechanical properties on condensate growth [11–14]. For example, elastic chromatin mechanics has been shown to frustrate the growth of nuclear condensates [13,14]. However, the combined impacts of macromolecular crowding, elastic networks, and nonequilibrium cellular activities on condensate formation are less well understood.

*Contact author: hockyg@nyu.edu

†Contact author: liam.holt@nyulangone.org

It is difficult to derive general physical principles from the study of endogenous condensates because these systems are formed through complex coacervation of many molecules. Furthermore, these components are often dynamically altered by post-translational regulation, the details of which are typically unknown. Thus, when perturbing intracellular environments, it is difficult to fully attribute structural changes in endogenous condensates to only biophysical cues, since biological functional changes associated with perturbations can also lead to structural changes in endogenous condensates. To overcome these issues, we developed an orthogonal synthetic intracellular condensate system, called synDrops. synDrops are adapted from a previous approach to create a molecular condensate of well-defined geometry [15], but with the added ability to chemically induce the interaction of components, thereby enabling kinetic analysis of condensate formation.

We successfully induced synDrop formation in both budding yeast *Saccharomyces cerevisiae* cells and mammalian cervical cancer HeLa cells. Complementary to the experimental system, we also developed two independent agent-based molecular dynamics models to simulate synDrops within cellular environments from first principles. Combining experiments and simulations, we show that macromolecular crowding facilitates the nucleation process while inhibiting the growth phase of condensate dynamics. However, ATP-dependent cellular activity promotes growth by assisting long-range structural rearrangements. In conclusion, we found that the assembly of mesoscale biomolecular condensates is favored by the crowded and active cellular environment.

II. RESULTS

A. Droplet dynamics can be captured using inducible synDrops in cells and in simulations

SynDrops are composed of two protein components, each of which has three modular domains. We based our design on the Flory-Stockmeyer theory [16], which governs polymer network growth. Multivalency is essential for the formation of mesoscale condensates through phase separation [17–21]. We used homomultimerizing domains to create multivalency in our system [Fig. 1(a)]. One component uses a homohexamer multimerization domain (PDB: 3BEY), and the other uses a homodimer domain (PDB: 4LTB). The two components interact in *trans* through two halves of an inducible heterodimeric binding interaction, enabling kinetic analysis. Importantly, the dimerization domain is a 19-nm-long, stiff, antiparallel coiled coil. Since the distance between interaction surfaces on the hexamer is approximately 6 nm, the dimer is sterically prevented from interacting with the same hexamer component more than once. Thus, geometric constraints strongly favor the expansion of synDrop molecular networks, which greatly simplifies simulation and physical analysis compared to other synthetic systems [19–21] [Fig. 1(a)].

Inducible binding is achieved using the plant GAI (Gibberellin insensitive DELLA proteins) and GID (Gibberellin Insensitive Dwarf 1) domains. These domains undergo a heterotypic interaction that is potentiated in the presence of the plant hormone Gibberellin (GA) [22] [Fig. 1(a)]. GAI was truncated to a minimum dimerization domain [23] and fused

to the hexamer component; the GID domain was fused to the dimer component. Adding GA increases the affinity between the two synDrop components and triggers synDrop formation.

We co-expressed these two proteins by integrating two plasmids into the genome in yeast cells, and through transient transfection in mammalian HeLa cells. Since the ratio between these two proteins is essential for condensate formation [15], we adapted our plasmid design for expression in mammalian cells by combining the two genes onto the same plasmid and separating them by a P2A ribosomal-skipping sequence [Fig. 1(b)]. The P2A sequence triggers ribosomal skipping, resulting in two independent proteins at equal expression levels [24]. After the proteins were expressed within cells, we added GA into the cell media and observed synDrop dynamics at different time points after GA addition [Fig. 1(d)]. Similar to previous reports [15], synDrops were spherical and were observed to fuse, suggesting they had liquidlike material properties [Fig. 1(c)].

Our *in vivo* system enables detailed analysis of mesoscale assembly, but cannot easily report on the microscopic protein interactions that underpin this process. Therefore, we developed two independent agent-based molecular dynamics (MD) platforms to provide complementary information *in silico*. The first simulation setup used a HOOMD-blue engine [25,26] combined with a dynamic bonding plugin that we previously developed [27] [Figs. 1(e) and 1(f); full parameters supplied in Table I], and the second used a custom-developed JAVA program (see Fig. 8 in Appendix A; full parameters supplied in Table II). The HOOMD-blue model uses GPU acceleration to increase simulation speeds, enabling us to investigate cluster formation dynamics over much longer timescales ($>10\times$), especially at high molecular density. However, we included results from both MD simulation models to ensure our simulation results were robust to variations in implementation details. In MD simulations with HOOMD-blue, we modeled the hexamer as a single sphere with six uniformly distributed binding sites, and the dimer as a rodlike structure formed from three spheres with two binding sites positioned on opposing sites of the two outer spheres [Fig. 1(e)]. In the JAVA MD simulations, we modeled the hexamer and dimer as spheres with six or two binding sites, respectively [Fig. 8(a) in Appendix A]. The sizes of these simulated structures were chosen based on crystal structure data from the Protein Data Bank (PDB) for the individual protein components within each protein complex. In addition, we included a third agent to mimic ribosomes, which are the dominant macromolecular crowders in the cytoplasm. This agent was a 30-nm-diameter sphere with no binding interactions. The formation of synDrops was simulated with or without crowders under equilibrium conditions [Figs. 1(f) and 8(b) in Appendix A]. There is a discrepancy in the timescales of synDrops formation between simulations and experiments. This could be due to various factors, such as the significantly smaller droplet sizes in simulations—approximately one-tenth the radius of those in the experimental system—and the simplified assumptions inherent in coarse-grained models representing cellular systems. In summary, we developed the synDrop system both in cells and *in silico*, allowing us to address how the intracellular environment affects the assembly of mesoscale condensates.

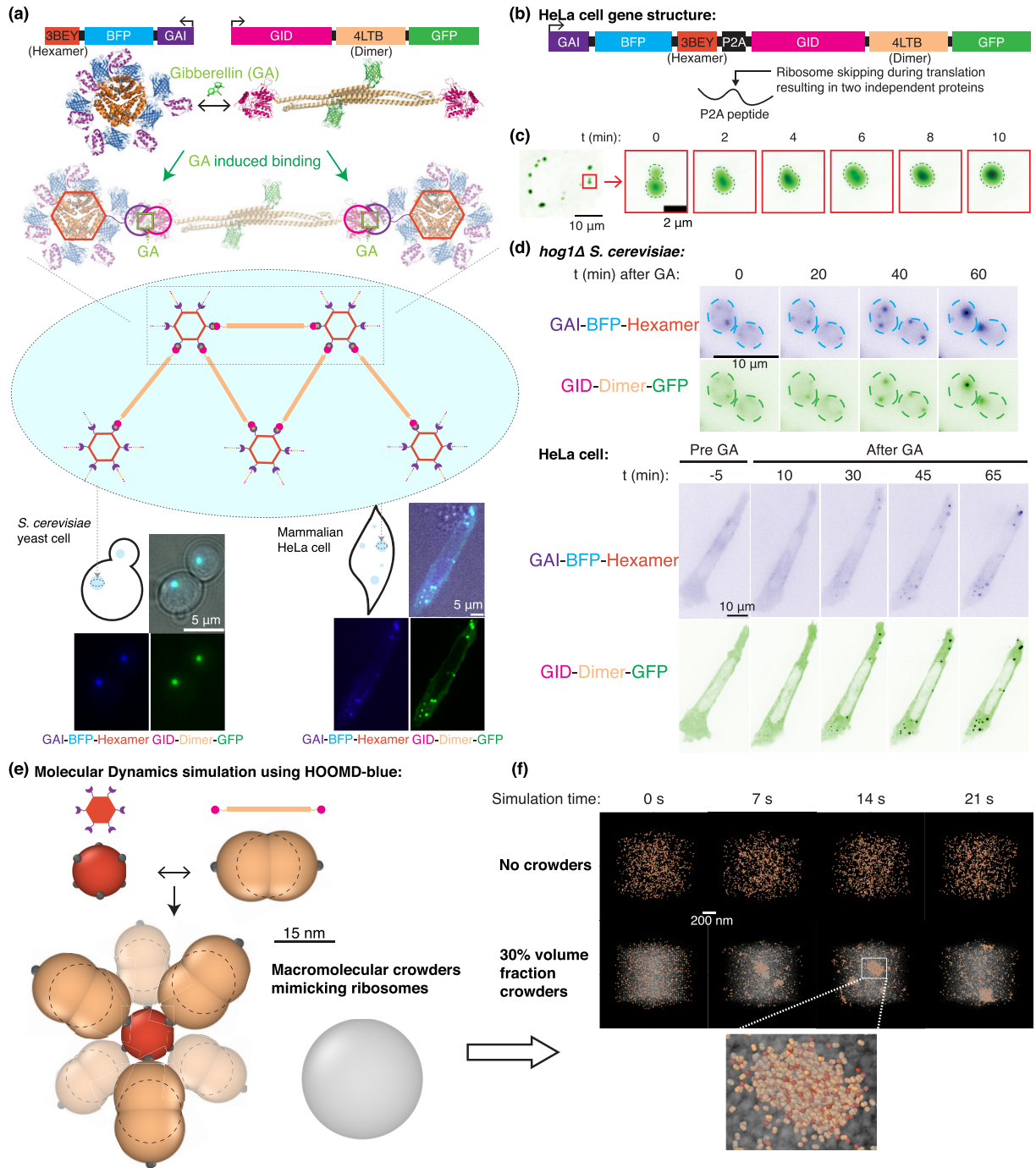


FIG. 1. synDrops enable the analysis of condensate formation kinetics in *S. cerevisiae* and mammalian cells, and are amenable to simulation. (a) synDrops are inducible synthetic condensates composed of two proteins. Top: Gene and crystal structures of the two components. Each protein has three domains: an oligomerization domain (hexamer [PDB: 3BEY] or dimer [PDB: 4LTB]), an inducible interaction domain (GAI or GID [PDB: 2ZSH]), and a fluorescent protein (BFP [PDB: 3M24] or GFP [PDB: 2B3P]). Bottom: Gibberellin (GA) induces binding between GAI and GID favoring the formation of a mesoscale molecular network (middle cartoon), as shown in representative images of both *S. cerevisiae* yeast cells and mammalian HeLa cells. (b) To efficiently express the two protein components of the synDrop system at similar levels in mammalian cells, the two open reading frames (ORFs) were connected by a P2A sequence. The two ORFs are translated one after the other from a single transcript due to ribosome skipping. (c) synDrops fuse within minutes, suggesting liquidlike properties. (d) GA addition leads to synDrop formation. Time course of synDrop formation in *hog1Δ S. cerevisiae* yeast cells, and mammalian HeLa cells. Scale bar, 10 μ m. (e) Schematic of molecular dynamics model for synDrop assembly. The hexamer component is represented by a sphere with six uniformly distributed binding sites; the dimer component is represented as a rodlike structure formed from three overlapping spheres with two binding sites positioned on opposite ends. A third component with no binding sites mimics ribosomes as macromolecular crowders. (f) Representative images from HOOMD-blue MD simulations of synDrops system over time without crowders (top) and with 30% volume fraction of crowders (bottom). The zoomed image under 30% volume fraction condition shows the formation of a large cluster.

TABLE I. Table of parameters for the MD simulations using HOOMD-blue.

Parameter (with description)	Value used in simulations
Simulation timestep (dt)	0.002
Crowder temperature T_c relative to $T_{\text{room}} = 298.15$ K	0.5–2.0
Simulation box length (nm)	860 (for the actual system) 400 (for the monomeric system to obtain K_d)
Number of rod proteins	1170 (for the actual system) 200 (for the monomeric system)
Number of hexamers	390 (for the actual system) 200 (for the monomeric system)
Number of GEMs	20
Number of binders on each hexamer	6
Number of binders on each rod	2
Volume fraction of ribosomes (crowders)	0.0–0.5
Diameter of inner rod particle (nm)	11.7
Diameter of the two outer rod particle(s) (nm)	13.45
Diameter of hexamer (nm)	12.6
Diameter of ribosome (nm)	30.0
Diameter of GEM (nm)	40.0
Diameter of binders on rods and hexamers (nm)	2.0
Maximum binding distance d_{bind} (nm)	1.0
Repulsion for soft quartic potential ($k_B T$)	500
ϵ for Lennard-Jones potential ($k_B T$)	0
Rate constant for dynamic binding k_{on} (units of $1/\tau$)	50.0
Rate constants for dynamic unbinding k_{off} (units of $1/\tau$)	0.001 (also 0.015, 0.006, 0.0003, 0.0001, 0.000015, 0.000002, 0.0000001, 0.000000007)
Binding affinity ϵ ($k_B T$)	10.8 (also 8.1, 9.0, 12.0, 13.1, 15.0, 17.0, 20.0, 25.0)

B. Macromolecular crowding promotes nucleation but inhibits droplet growth

We examined synDrop kinetics within cells under various conditions using fluorescence microscopy. We first characterized GA-induced droplet dynamics in yeast cells by quantifying the average number of droplets per cell, as well as total intensity per droplet (see Sec. IV G). Changes in total intensity per droplet are indicative of changes in cluster size and/or its molecular density. Droplet growth occurred in two phases. First, there was a nucleation phase, during which the average droplet number per cell increased. Subsequently, droplets grew by fusion and coarsening, leading to a decrease in droplet number and an increase in droplet intensity.

TABLE II. Table of parameters for the MD simulations using custom-developed JAVA program.

Parameter (with description)	Value used in simulations
Simulation timestep (dt) (s)	10^{-7}
Crowder temperature T_c relative to $T_{\text{room}} = 298.15$ K	1.0
Viscosity (Pa s)	0.03
Simulation box length (nm)	860 (for the actual system) 400 (for the monomeric system to obtain K_d)
Number of rod proteins	1170 (for the actual system) 200 (for the monomeric system)
Number of hexamers	390 (for the actual system) 200 (for the monomeric system)
Number of binders on each hexamer	6
Number of binders on each rod	2
Volume fraction of ribosomes (crowders)	0.0–0.5
Diameter of rod (nm)	23.4
Diameter of hexamer (nm)	12.6
Diameter of ribosome (nm)	30.0
Maximum binding distance d_{bind} (nm)	2.3
Rate constants for dynamic unbinding (k_{off}) (s^{-1})	26

Under control conditions with only yeast growth media of synthetic complete dextrose (SCD), we observed an increase in droplet number within the first 10 min after inducing binding interactions by the addition of GA [gray curve, Fig. 2(a)]. However, the total intensities of these newly formed individual droplets did not grow during this period [Fig. 2(b)]. This suggests that droplets initially nucleate locally but do not grow substantially. After 10 min, the droplet number started to decrease and the intensity started to increase. However, the normalized total intensities of all droplets per cell (see Fig. 10 in Appendix B) fluctuated around a stable value. This corresponds to a growth phase where droplet sizes become larger, mainly through droplet coalescence. Thus, the synDrops system forms droplets by nucleation and growth, which has been suggested to be the most common mechanism of endogenous condensate formation [28,29].

We next explored the effects of macromolecular crowding on synDrop formation. Osmotic compression of cells can increase macromolecular crowding. However, wild-type (WT) yeast can rapidly balance external osmotic pressure by producing glycerol [30]. To circumvent osmo-adaptation in yeast cells, we used *hog1* Δ yeast cells [Fig. 1(d)]. Hog1p is a key regulator kinase, required for rapid accumulation of the osmolyte glycerol in yeast cells [30]. Deletion of the *HOG1* gene prevents rapid osmo-adaptation, allowing us to more precisely tune molecular crowding; we used *hog1* Δ *S. cerevisiae* strains in this study unless otherwise stated.

After osmotic compression, the initial number of droplets nucleated was increased compared to control [yellow and

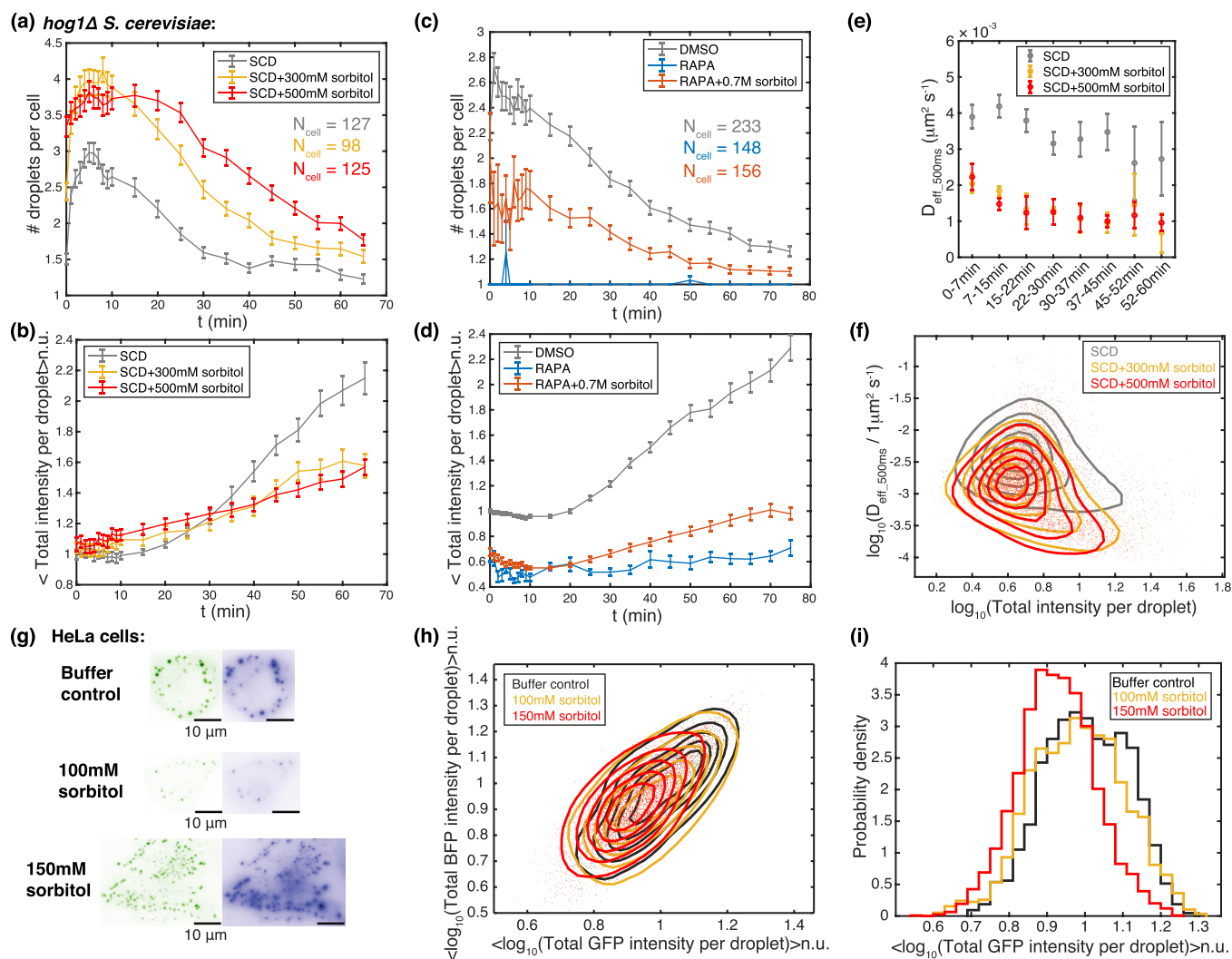


FIG. 2. Increasing molecular crowding promotes synDrop nucleation but inhibits growth. (a) Average number of droplets per cell (*hog1Δ S. cerevisiae*) for 1 hour after synDrop induction with GA for control (SCD, synthetic complete dextrose media, which is the yeast growth media) and two osmotic compression conditions (adding sorbitol). Error bars are standard error of the mean (SEM). (b) Total intensities per droplet normalized to the mean value of droplets in control cells at 0 min. Data are mean \pm SEM. (c) Average number of droplets per cell and (d) normalized total intensity per droplet over 1 hour comparing control (DMSO) and decreased molecular crowding (rapamycin, RAPA) conditions, as well as RAPA treatment with recovered molecular crowding (RAPA + 700 mM sorbitol). Data are mean \pm SEM. (e) Median diffusivity of droplets at different time points postinduction in the same conditions as (a) and (b). Error bars are SEM. (f) Density plot of droplet diffusivity versus total intensity per droplet at all time points postinduction. [(g)–(i)] synDrops formed in mammalian HeLa cells after 1–2 hours of induction comparing control to osmotic compression conditions (100 or 150 mM sorbitol). (g) Representative images, scale bar 10 μm . (h) Phase diagram of synDrop formation as a function of total BFP and GFP intensities per droplet, normalized to the median value of droplets in the buffer control condition. (i) Histogram of normalized total GFP intensities per droplet (logarithmic scale).

red curve, Fig. 2(a)]. However, the subsequent increase in droplet intensities was suppressed [yellow and red curve, Fig. 2(b)]. Similar results were also obtained in WT yeast cells before osmo-adaptation started to have an effect (see Fig. 11 in Appendix C). This suggests that macromolecular crowding promotes synDrop nucleation but inhibits growth.

Besides increasing macromolecular crowding, osmotic compression also increases the concentrations of the protein components [Fig. 12(a) in Appendix C]. We took advantage of the noise in protein expression levels in single cells to evaluate the relative importance of increased protein

concentration versus increased molecular crowding in changing synDrop dynamics. We first grouped cells in each condition (control and osmotic compression conditions) into four quantiles based on their cellular mean pixel intensities before GA induction, indicating protein expression levels. By quantifying the average number of droplets per cell within different cell quantiles for each condition, we observed that in all conditions, the number of droplets per cell was higher in cell groups with higher intensities (fourth quartile) and lower in cell groups with lower intensities (first quartile) when compared to the overall average for all cells [Fig. 12(b) in Appendix C]. This confirms that protein concentrations affect

synDrop formation. However, if we compared control cells to compressed cells within the same range of protein concentrations, we obtained qualitatively similar results to Figs. 2(a) and 2(b) [Fig. 12(c) in Appendix C]. These results indicate that the effects of osmotic compression on synDrop assembly kinetics is mainly due to increased macromolecular crowding.

We sought orthogonal means to change macromolecular crowding. Ribosomes are the dominant mesoscale crowders in the cytoplasm, where they take up around 20% of the volume (about half of the total volume excluded by macromolecules) [2]. It has been shown that ribosome concentrations are tuned through the TORC1 (target of rapamycin complex 1) pathway [2]. Inhibition of TORC1 using rapamycin reduces ribosome biogenesis and increases ribosome degradation, leading to lower ribosome concentration and therefore reduced macromolecular crowding. We treated yeast cells with either rapamycin or DMSO (solvent control) for 2 hours. We found rapamycin-treated cells did not form droplets after GA induction [Figs. 2(c), 2(d), and 13(a) in Appendix D]. However, GFP signal was reduced after rapamycin treatment [Fig. 13(c) in Appendix D]. Thus, rapamycin treatment reduced the concentration of the dimer component, likely due to increased cell size and decreased protein translation upon TORC1 inhibition [31]. We again wished to determine how changes in macromolecular crowding and in protein concentration each impacted synDrop assembly. To achieve this, we sought to restore normal macromolecular crowding in rapamycin-treated cells. We leveraged a microrheology approach with genetically encoded multimeric nanoparticles (GEMs) to quantify crowding [2]. We found that macromolecular crowding was decreased in rapamycin-treated cells, consistent with previous reports [2] [Fig. 13(b) in Appendix D]. We then osmotically compressed [Fig. 13(b) in Appendix D], and found that 0.7 M sorbitol restored macromolecular crowding of rapamycin-treated cells to the level of control cells [Fig. 13(b) in Appendix D]. However, this level of osmotic compression barely altered protein concentrations [Fig. 13(c) in Appendix D]. In these conditions, we found that synDrop formation was recovered [Figs. 2(c), 2(d), and 13(a) in Appendix D], but resulted in the formation of fewer and smaller droplets over the same time course. These results further indicate that macromolecular crowding is crucial for synDrop assembly and protein concentrations are also important.

We next examined the mechanisms underlying the inhibition of droplet growth by macromolecular crowding. Droplets can grow in two ways: through droplet coalescence [32] and/or through Ostwald ripening [33]. However, droplet coalescence has been suggested to be the dominant mechanism for droplet growth in biological systems [13]. In this mechanism, the rate of droplet growth depends on the collision rate between two smaller droplets, which in turn depends on the diffusivities of these droplets [13,32]. The kinetics of synDrop formation were also consistent with a mechanism dominated by coalescence (Fig. 10 in Appendix B). We therefore hypothesized that macromolecular crowding could inhibit droplet growth by reducing droplet diffusivities. To test this hypothesis, we quantified synDrop diffusivities through particle tracking in both control conditions and after increasing macromolecular crowding. Since droplet size increases with time,

we analyzed droplet diffusivities at different time points after induction. We found that droplets diffused more slowly after osmotic compression compared to control [Fig. 2(e)]. Droplet diffusivity depends upon the environment and droplet size. However, average total intensities per droplet were lower in osmotic compression conditions, indicating that the reduction in droplet diffusivities was not due to increased droplet size [Fig. 2(f)]. These results support our hypothesis that macromolecular crowding reduces droplet diffusivities and thus inhibits droplet growth.

To investigate if the effects of the cellular environment were conserved in human cells, we transfected plasmids encoding the two synDrop components into HeLa cells. We observed the formation of droplets [Fig. 2(g)]. The amount of DNA delivered to cells is highly variable in transient transfection and, as a result, protein expression levels were highly variable in these experiments. Since protein concentration affects the kinetics of droplet formation, this heterogeneity in protein expression levels across the population made it challenging to study averaged droplet kinetics effectively. Instead, we took advantage of this heterogeneity to define a phase diagram based on the total intensities of two protein components for each droplet at a fixed time point [Fig. 2(h)].

First, we tested the effects of increasing molecular crowding through osmotic compression. Similar to yeast, we observed a decrease in droplet size and an increase in droplet number per cell after osmotic compression [Figs. 2(g) and 2(h)]. We found the synDrops formed in the same region of the phase diagram regardless of the experimental condition, suggesting that a specific amount and ratio of protein components is required for synDrop formation, as predicted for a process driven by phase separation [Fig. 2(h)]. However, droplet intensities were lower after osmotic compression compared to control [Figs. 2(h) and 2(i)]. Therefore, we conclude that macromolecular crowding inhibits droplet growth in both human and yeast cells.

Next, we employed our agent-based (MD) models to simulate synDrops. These models allowed us to investigate molecular details that are not easily accessible from experimental data. The well-defined structures and binding interactions between the two synDrop components allowed us to quantify droplet network structures with graph-theory-based analyses [Fig. 3(a)]. Unless otherwise specified, the concentrations of dimer and hexamer synDrop components remain at 3 and 1 μM , respectively, in the following simulations. Here, we defined each synDrop component as a node and the bond between two components as an edge. We calculated the topological shortest distances between each pair of components and mapped out bond connectivity to define each molecular cluster. The distance matrix from this analysis was then used for hierarchical clustering [34]. Within the resulting clustergram, squares along the diagonal correspond to clusters of interacting molecules. Each pixel on the x and y axes represents an interaction between two individual molecules in the simulation system and is colored according to the topological distance between them (e.g., molecules that are directly connected are dark blue, while molecules that are indirectly connected through a chain of interactions are a lighter hue). Blank pixels indicate that there is no path connecting the two corresponding molecules [Figs. 3(a), 3(c),

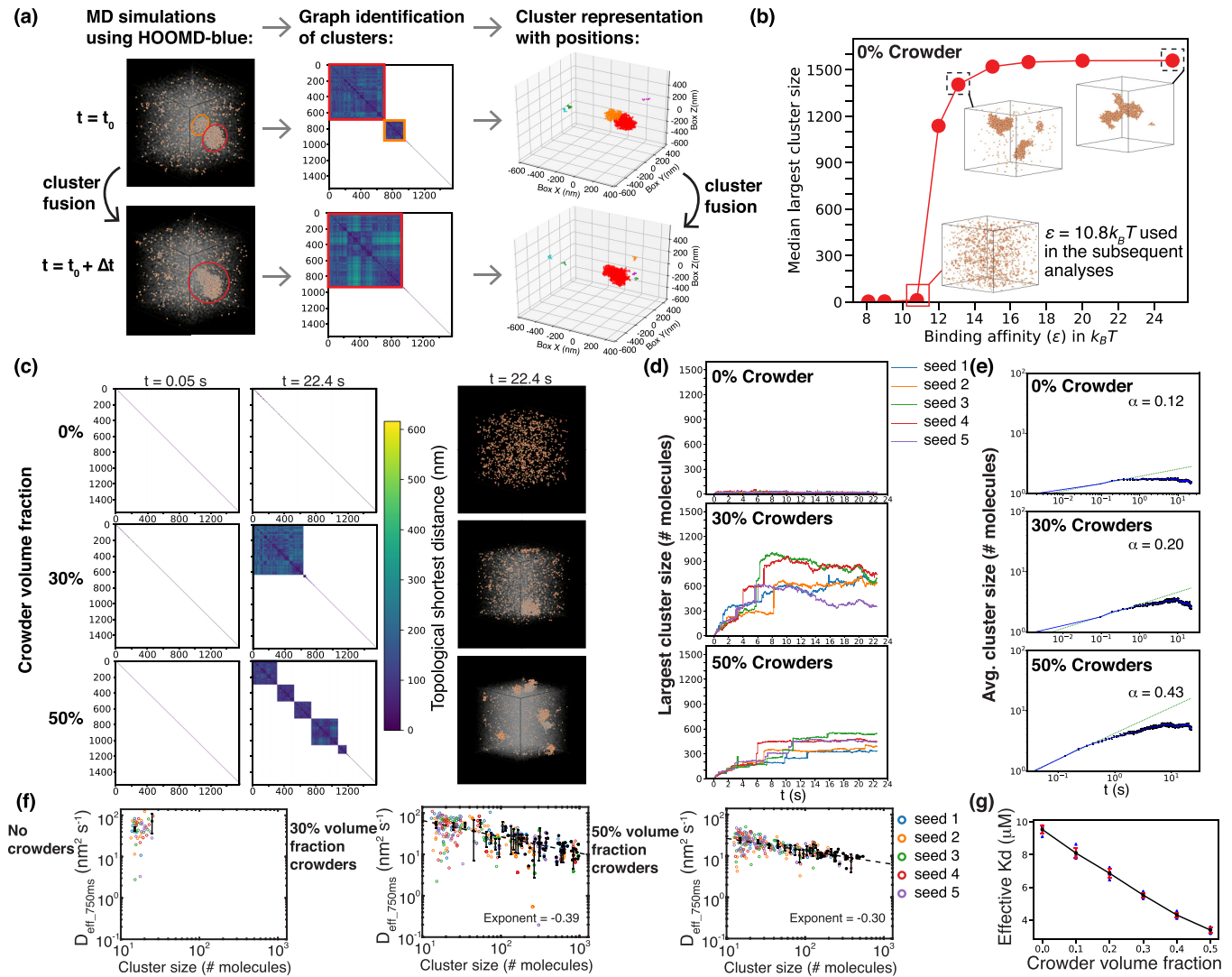


FIG. 3. Increasing molecular crowding promotes synDrop nucleation but inhibits growth. (a) Illustration of graph-theory-based analyses on cluster formations, showing the cluster fusion process as an example. Extracted from MD simulation data (left), the positions and binding information of synDrop components are utilized to generate a distance matrix reflecting the topological shortest distances between each component pair. Through hierarchical clustering of this distance matrix, the clusters are both identified in a clustergram (middle) and represented spatially (right). (b) Median largest cluster sizes among five repeats plotted as a function of the binding affinity ϵ between two synDrop components at 0% volume fraction of crowders. Representative snapshots are shown for binding affinities $10.8k_B T$, $13.1k_B T$, and $25.0k_B T$, indicative of an abrupt increase in cluster formation observed between binding affinities $11k_B T$ and $12k_B T$. The binding affinity ϵ was varied by changing the unbinding rate constant k_{off} , keeping the binding rate constant k_{on} fixed. The binding affinity of $10.8k_B T$ was used for all subsequent analyses. [(c)–(g)] Analyses of MD simulations using HOOMD-blue comparing conditions with 0%, 30%, and 50% volume fractions of crowder: (c) Graph theory analyses (left) of cluster formation at early and later times with corresponding simulation renderings (right) under three crowder volume fractions: 0% (top), 30% (middle), and 50% (bottom). (d) Number of molecules within the largest cluster over time from five replicate simulations. Each replicate is denoted by “seed.” (e) Average cluster size (number of molecules) over time from five replicate simulations. The dashed line represents the power-law fit for the initial 0.5 s, exponent denoted as α . Error bars are standard deviation (SD) of the average values of five repeats. (f) Cluster diffusivity versus cluster size (number of molecules) on the log-log scale from five replicate simulations, denoted as “seed.” The black data points represent the mean of averaged values from five repeats with a bin size of 10, and the error bars correspond to the SD among these averaged values. The dashed black line represents the linear fit on the log-log scale and the fitted slope is labeled as the exponent. (g) Effective dissociation constants (K_d) of a simplified monovalent system as a function of crowder volume fraction. Error bars are SD from five repeats for a given crowder volume fraction.

and 9(a) in Appendix A]. Squares on the diagonal correspond to condensates: The red and orange clusters circled in the simulation snapshot [Fig. 3(a), left] and in the three-dimensional (3D) graph [Fig. 3(a), right] were identified from the blocks of interactions highlighted by red and orange in the

clustergram [Fig. 3(a), middle]. Next, we determined how the largest cluster size changed as a function of binding affinity (see Fig. 14 in Appendix E). All simulations were run to the same time point, where the largest cluster sizes mostly converged. We then extracted the median values of five repeats

at the final time point to plot Fig. 3(b), and observed an abrupt increase in cluster formation at a binding affinity of around $11k_B T - 12k_B T$ [Fig. 3(b)]. To capture the full dynamic range of the system, we chose a binding affinity near the transition range, specifically $10.8k_B T$, for all subsequent MD simulation analyses.

When there were no crowders in the system, there was very limited cluster formation (Fig. 3(c), top; Fig. 9(a) in Appendix A, top; see Supplemental Material [35]). In contrast, large clusters formed when a 30% volume fraction of crowder was added to mimic the excluded volume typically present in the cytoplasm, suggesting that macromolecular crowding can be crucial to nucleate and stabilize synDrop mesoscale networks (Fig. 3(c), middle; Fig. 9(a) in Appendix A, middle; see Supplemental Material [35]). However, when we further increased the crowder volume fraction to 50% (mimicking crowder concentrations in osmotically compressed cells), we observed a larger number of smaller droplets (Fig. 3(c), bottom; Fig. 9(a) in Appendix A, bottom; see Supplemental Material [35]). Similar results were also obtained by tracking the number of molecules within the largest cluster [Figs. 3(d) and 9(b) in Appendix A] and by plotting the cluster size distribution at the end time point [Fig. 9(d) in Appendix A]. The initial growth rate of average cluster size increased with crowder volume fraction [Figs. 3(e) and 9(c) in Appendix A], suggesting that nucleation was promoted by macromolecular crowding. However, under high crowding conditions (e.g., 50% volume fraction) cluster size was limited at late time points. These results are consistent with our experimental data that physiological crowding ($\sim 30\text{--}35\%$) appears to be optimal for the formation of large synDrops. Molecular crowding plays contrasting roles in droplet nucleation and growth. While it is crucial for droplet nucleation, it also inhibits droplet growth.

To further investigate the molecular basis of frustrated synDrop growth in the presence of excessive macromolecular crowding, we plotted the average diffusivity for each cluster as a function of the cluster size. We found that diffusivities decreased as a function of cluster size as expected, and were reduced overall when crowder volume fractions were increased [Figs. 3(f) and 9(e) in Appendix A], consistent with our hypothesis that crowding frustrates coalescence by reducing cluster diffusivities. This effect is particularly pronounced under conditions of excess macromolecular crowding.

Finally, we investigated the molecular basis of the promotion of droplet nucleation by macromolecular crowding. We hypothesized that increased macromolecular crowding could favor binding interactions, as previously reported [5,36]. To assess this idea, we performed MD simulations on a simplified system where two protein components each had only a single available binding site (1,1) [Fig. 9(f) in Appendix A]. The rationale of using a monovalent system here rather than the full synDrop system was to exclude other factors that affect calculations of chemical bond properties, such as changes in coordination numbers for hexamers and dimers, which increase with crowding (see Fig. 15 in Appendix E). We then extracted the effective dissociation constant (K_d) under different volume fractions of crowders by quantifying the number of bonds formed at equilibrium. The effective K_d was

indeed reduced (affinity was increased) in simulations with increased crowder volume fractions [Figs. 3(g) and 9(g) in Appendix A]. Furthermore, we determined the unbinding rate (k_{off}) by allowing the system to reach equilibrium, switching the binding rate to zero, and then measuring the rate at which bonds dissociate [Fig. 9(f) in Appendix A]. Calculation of effective K_d and k_{off} allowed us to infer the effective binding rate (k_{on}), which is k_{off} divided by K_d . Interestingly, when comparing conditions with 30% volume fraction crowder to those with no crowders, we found that k_{off} did not change [Fig. 9(f) in Appendix A]. This indicates that the decrease in effective K_d is mainly attributed to an increase in effective k_{on} , potentially facilitated by the increase in effective concentration.

In conclusion, our combination of *in vivo* experiments and simulations supports the model that macromolecular crowding promotes droplet nucleation by reducing the effective K_d for chemical bond formation, but also inhibits droplet growth by reducing droplet diffusivity, therefore kinetically frustrating coalescence of small droplets into larger structures.

C. ATP-dependent cellular activities promote droplet growth

We wondered if features of the cytoplasmic environment other than macromolecular crowding could impact synDrop assembly. In addition to being crowded, the cytoplasm is also far from equilibrium due to ATP-dependent activities. Cellular metabolism was previously shown to strongly affect the motion of mesoscale particles [37]. We therefore hypothesized that ATP-dependent cellular activities might affect synDrop formation by promoting their motion and therefore driving coalescence of small droplets into larger structures.

We used metabolic inhibitors: 2-deoxyglucose (2-DG) and antimycin were used to deplete intracellular ATP in yeast cells, taking care to maintain neutral pH within cells and isotonic conditions to avoid osmotic perturbations to cell volume [38]. We depleted ATP at different time points to assess the importance of ATP during different phases of synDrop assembly. We observed that synDrop growth was inhibited within 10 min of ATP depletion [Fig. 4(a), top], and synDrop diffusivity was also reduced immediately after ATP depletion [Fig. 4(a), bottom]. These effects were most apparent when ATP was depleted early during synDrop assembly [Fig. 4(b)]. Therefore, cellular active matter is crucial for both synDrop diffusivity and growth in yeast cells.

We repeated this experiment in HeLa cells, and found that droplet diffusivity was greatly reduced after we removed all metabolic activity by ATP depletion [Fig. 4(c)]. The dynamics of the actomyosin cytoskeleton are an important source of cellular motion [39]. We therefore hypothesized that actomyosin contractility might agitate the cytoplasm and increase synDrop motion. To test this idea, we inhibited actomyosin dynamics using the JLY drug cocktail, which simultaneously prevents actin depolymerization, polymerization, and myosin II-based restructuring [40]. This treatment reduced diffusivity almost as much as total ATP depletion, suggesting that actomyosin dynamics is the dominant mechanism that increases mesoscale diffusivity in the cytoplasm of mammalian cells [Fig. 4(c)]. Depletion of ATP or freezing of actomyosin dynamics using JLY decreased both droplet diffusivity and

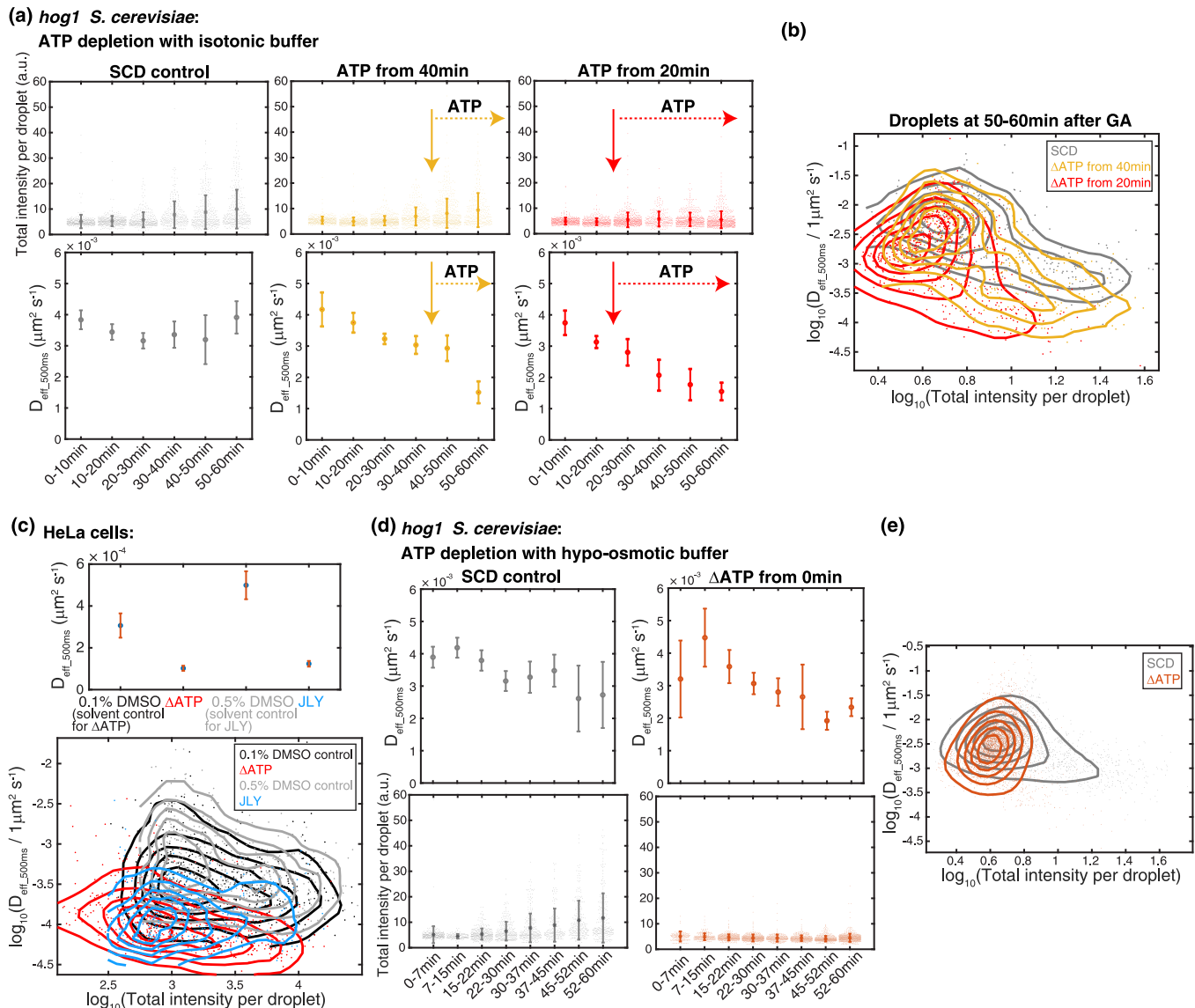


FIG. 4. ATP depletion inhibits synDrop growth. (a) Droplet formation in *hog1* Δ *S. cerevisiae* yeast cells in control conditions and after ATP depletion with an isotonic buffer using 80 mM sorbitol. ATP was depleted from two time points (indicated by arrows), 20 and 40 min after synDrop induction with GA: (top) total intensity per droplet, mean \pm SD; (bottom) median droplet diffusivity \pm SEM. (b) Density plot of individual droplet diffusivity versus its total intensity 50–60 min after induction. (c) Properties of droplets that were preformed by 1 hour of GA induction with DMSO (solvent control) in mammalian HeLa cells and subsequently treated with the following conditions for 1 hour: ATP depletion, or the JLY cocktail (which freezes actomyosin dynamics). (top) Median droplet diffusivity \pm SEM; (bottom) density plot of diffusivity versus total intensity for individual droplets. (d) Droplet formation in *hog1* Δ *S. cerevisiae* yeast cells comparing control conditions to ATP depletion with a hypo-osmotic buffer using 10 mM sorbitol: (top) median droplet diffusivity. Error bars are SEM; (bottom) total intensity per droplet: averaged values \pm SD. (e) Density plot of diffusivity versus total intensity for individual droplets at all time points postinduction.

droplet intensity [Fig. 4(c), bottom]; however, it remains unclear whether droplet size was only determined by droplet diffusivity in these cases. In conclusion, actomyosin activity is the dominant ATP-dependent activity that increases synDrop motion in mammalian cells and is required for the formation of large synDrops.

We next tested whether reduced diffusivity of synDrops is the main cause of growth inhibition upon ATP depletion. To do so, we used hypo-osmotic shock to drive water influx and reduce crowding until the diffusivity of synDrops in ATP-depleted cells was the same as that of untreated cells [Fig. 4(d), top, and Fig. 4(e)]. However, droplet growth was

still inhibited in ATP-depleted cells, even when diffusivity was restored [Fig. 4(d), bottom, and Fig. 4(e)]. This result suggested that increasing droplet diffusivity at short timescales and length scales was insufficient to rescue synDrop growth. Therefore, we conclude that additional ATP-dependent cellular activities are necessary to promote synDrop growth.

Next, we attempted to model the role of cellular active matter using our MD simulations. To achieve this, we used a simple approximation of altered environmental motion by adding frequency-independent isotropic noise to vary the effective temperature of crowders [41,42] while keeping the

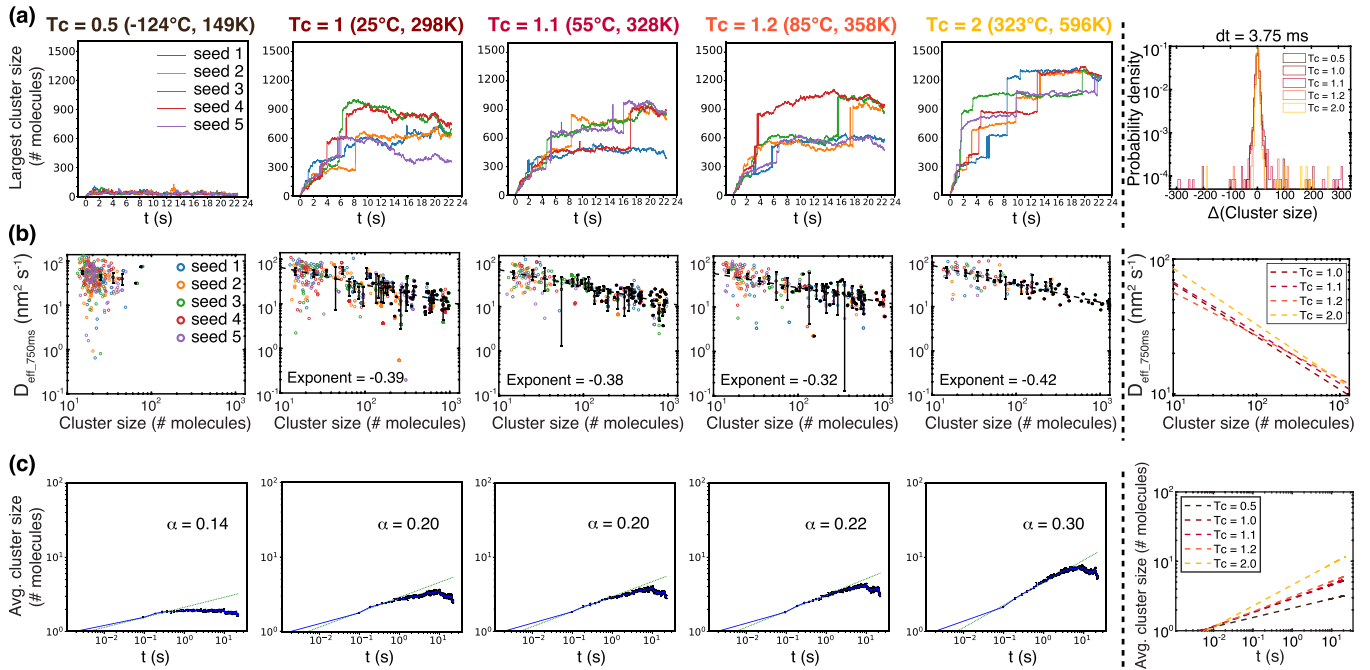


FIG. 5. Increasing the effective temperature of crowders promotes cluster growth in MD simulations. [(a)–(c)] MD simulations using HOOMD-blue with a constant 30% crowder volume fraction but varying crowder effective temperatures T_c . Values are shown relative to room temperature (298 K): 0.5, 1, 1.1, 1.2, 2. (a) Left: Number of molecules within the largest synDrop cluster over time from five replicate simulations, denoted by “seed.” Right: Distribution of probability density illustrating changes in the sizes of the largest clusters over a short time interval of 3.75 ms. (b) Left: Cluster diffusivity versus cluster size (number of molecules) from five replicate simulations, denoted by “seed.” The black data points are the mean of five replicate simulations with a bin size of 10, error bars are SD, dashed black line is the linear fit in logarithmic space with exponent (slope) labeled. Right: Overlay of linear fitted lines in logarithmic space for four T_c conditions, excluding the lowest T_c condition ($T_c = 0.5$). (c) Left: Average cluster size (number of molecules) over time from five replicate simulations. The dashed line represents the power-law fit for the initial 0.5 s, with the value of the exponent α indicated. Error bars are SD of the averaged values from the five repeats. Right: Overlay of power-law fitted lines for all five T_c conditions.

temperature of the synDrop components constant. We observed a positive correlation between the largest cluster size and the effective temperature of the crowders [Fig. 5(a), left]. We also quantified the frequency of synDrop cluster size change within a short time interval. At higher effective temperature, we observed a greater incidence of positive changes in cluster size and a reduced frequency of negative changes [Fig. 5(a), right]. When we plotted cluster diffusivity versus cluster size on a log-log scale, we observed individual cluster diffusivities were slightly higher with higher effective crowder temperatures [Fig. 5(b)]. However, this increase in cluster diffusivity was relatively modest, implying that other factors may contribute more significantly to the increased mesoscale assembly at higher crowder effective temperature. In particular, we found the initial growth rate of average cluster size was more rapid at higher crowder effective temperatures [Fig. 5(c)]. Since this initial growth rate is minimally impacted by cluster diffusivity, we think this increase in cluster sizes with respect to crowder effective temperature. It is important to note that while the results may appear similar between simulations and experiments, the underlying contributing factors differ. This is because the simplified assumptions in MD simulations cannot fully replicate the complex dynamics of the cytoplasm, such as changes in cytoplasmic elasticity and active rearrangements of cytoskeletal networks.

D. ATP-dependent cellular activities facilitate droplet growth by promoting long-range cellular structural reorganization

Given that coalescence dominates synDrop growth, the growth process is intrinsically linked to droplet motion, at both short and long timescales and length scales. Multiple intracellular factors can influence droplet motion, including macromolecular crowding, viscoelasticity, and poroelasticity [43]. Nonequilibrium ATP-dependent cellular activities can modify all of these factors. At small length scales (<100 nm), ATP-dependent cellular activities may change the spatial distribution and dynamics of macromolecular crowders. At larger length scales (>100 nm), cellular structures including membranes and the actomyosin cytoskeleton, both of which undergo dynamic ATP-dependent fluctuations, have strong impacts on mesoscale confinement and elasticity [39,44]. We therefore examined droplet trajectories more closely to gain insight into how long-range confinement and elasticity relate to synDrop growth.

The average distributions of angles between two vectors that connect subsequent steps in particle tracks can indicate whether particles are driven by active motion, or confined. The angle correlation function is calculated from the ensemble- and time-averaged cosine values of droplet trajectory angles at various time lags [45]. In the ideal case of pure Brownian motion, angles are randomly distributed and the angular correlation function is zero. However, if the average angle

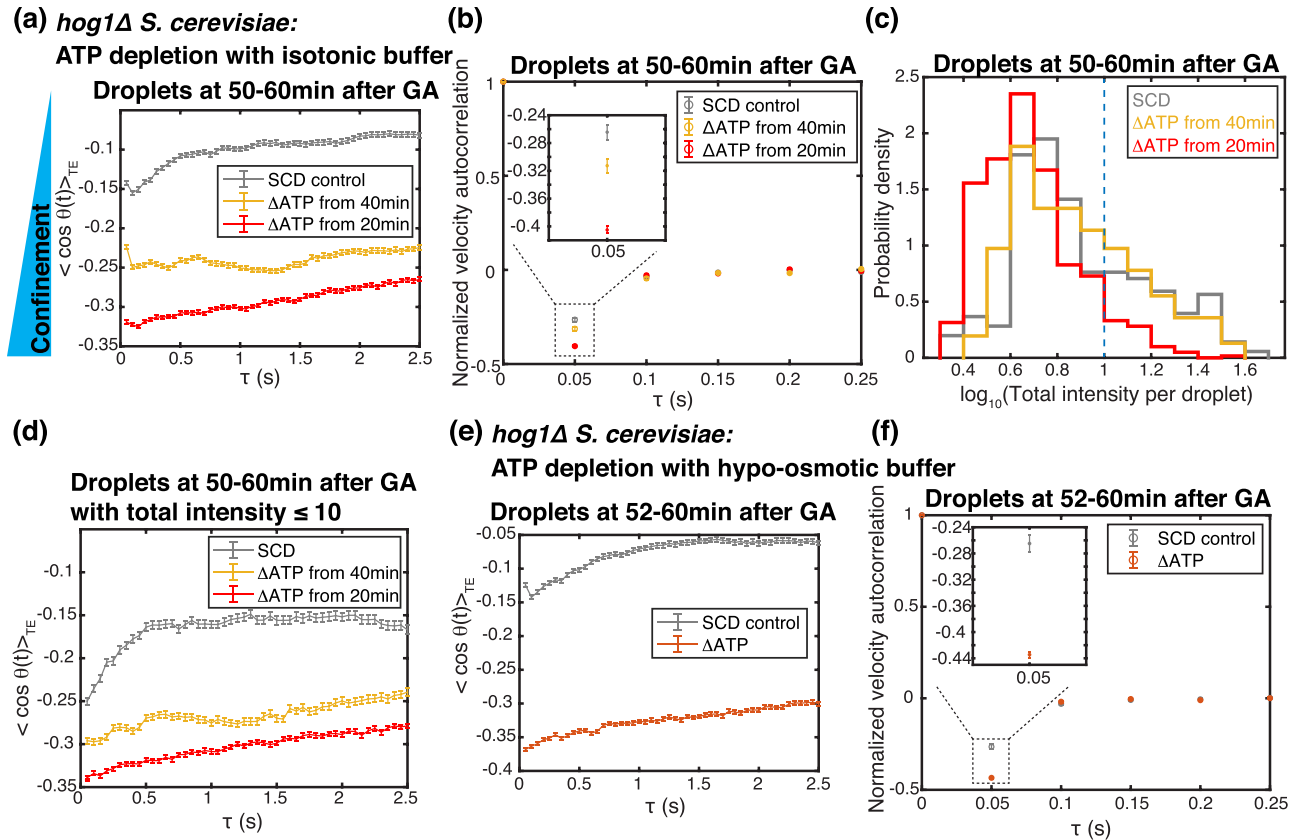


FIG. 6. ATP-dependent cellular activity facilitates droplet growth by promoting long-range cellular structural reorganization. (a) Angle correlation analyses on droplet trajectories at 50–60 min after synDrop induction with GA in *hog1Δ S. cerevisiae* yeast cells comparing control conditions to ATP depletion with an isotonic buffer from 20 and 40 min. Lower angle correlation values indicate greater confinement. (b) Normalized velocity autocorrelation for droplet trajectories in *hog1Δ S. cerevisiae* yeast cells. Droplets were analyzed 50–60 min after synDrop induction. (c) Histogram of total intensity per droplet at 50–60 min after synDrop induction with GA in *hog1Δ S. cerevisiae* yeast cells in control conditions or after ATP depletion with isotonic buffer from 20 and 40 min after synDrop induction. Droplets with a total intensity ≤ 10 (blue dashed line) were analyzed in (d). (d) Angle correlation analyses of droplets with total intensity ≤ 10 . (e) Angle correlation analyses of droplet trajectories at 52–60 min after synDrop induction in *hog1Δ S. cerevisiae* yeast cells comparing controls to ATP depletion with a hypo-osmotic buffer (simultaneous with synDrop induction). (f) Normalized velocity autocorrelation for droplet trajectories at 52–60 min after synDrop induction in *hog1Δ S. cerevisiae* yeast cells using the same conditions as (e).

between steps is in the range of $\pi/2$ to π , the angular correlation function will be less than zero (-1 to 0). This indicates antipersistent motion in particle trajectories, suggesting confined or caged particle movement. Conversely, if the averaged angle between steps falls in the range of 0 to $\pi/2$, the angular correlation function will be larger than zero (0 to 1). This implies persistent motion in particle trajectories, suggesting motion driven by active processes. We analyzed trajectories of synDrops formed 50–60 min after induction in control conditions or after ATP depletion in an isotonic buffer in yeast cells [Fig. 6(a)]. We observed negative angle correlations at all timescales, indicating confined motion. This confinement was most apparent at short timescales. Angle correlation values were further reduced when ATP was depleted for a longer time, suggesting that particles experienced higher confinement. We conclude that ATP-dependent activities reduce confinement in the cytoplasm.

We further investigated the origin of this confinement by quantifying the cytoplasmic elasticity using the velocity autocorrelation function [46] of the droplet trajectories.

In the ideal case of pure Brownian motion, the velocity autocorrelation function is zero. We focused on the same set of droplets as in Fig. 6(a) in both control conditions and ATP depletion in an isotonic buffer [Fig. 6(b)]. We observed a negative peak, corresponding to antipersistent particle motion, which is a signature of elastic materials. The magnitude of this negative peak increased after ATP depletion, and this elasticity further increased after longer periods of ATP depletion [Fig. 6(b), inset]. This suggests that ATP depletion increases the elasticity of the cytosol. This elasticity may impede mesoscale droplet motion and thus impose a long-range confinement. We conclude that ATP-dependent cellular activities help reduce cellular elasticity, fluidize the cytosol, and constantly remodel the cytosol to reduce confinement, leading to increased mesoscale droplet motion, which promotes droplet growth.

To enable more precise comparison between conditions, and avoid the concern that the distribution of synDrop sizes changes in different conditions, we selected droplets present at 50–60 min after synDrop induction that had similar intensities

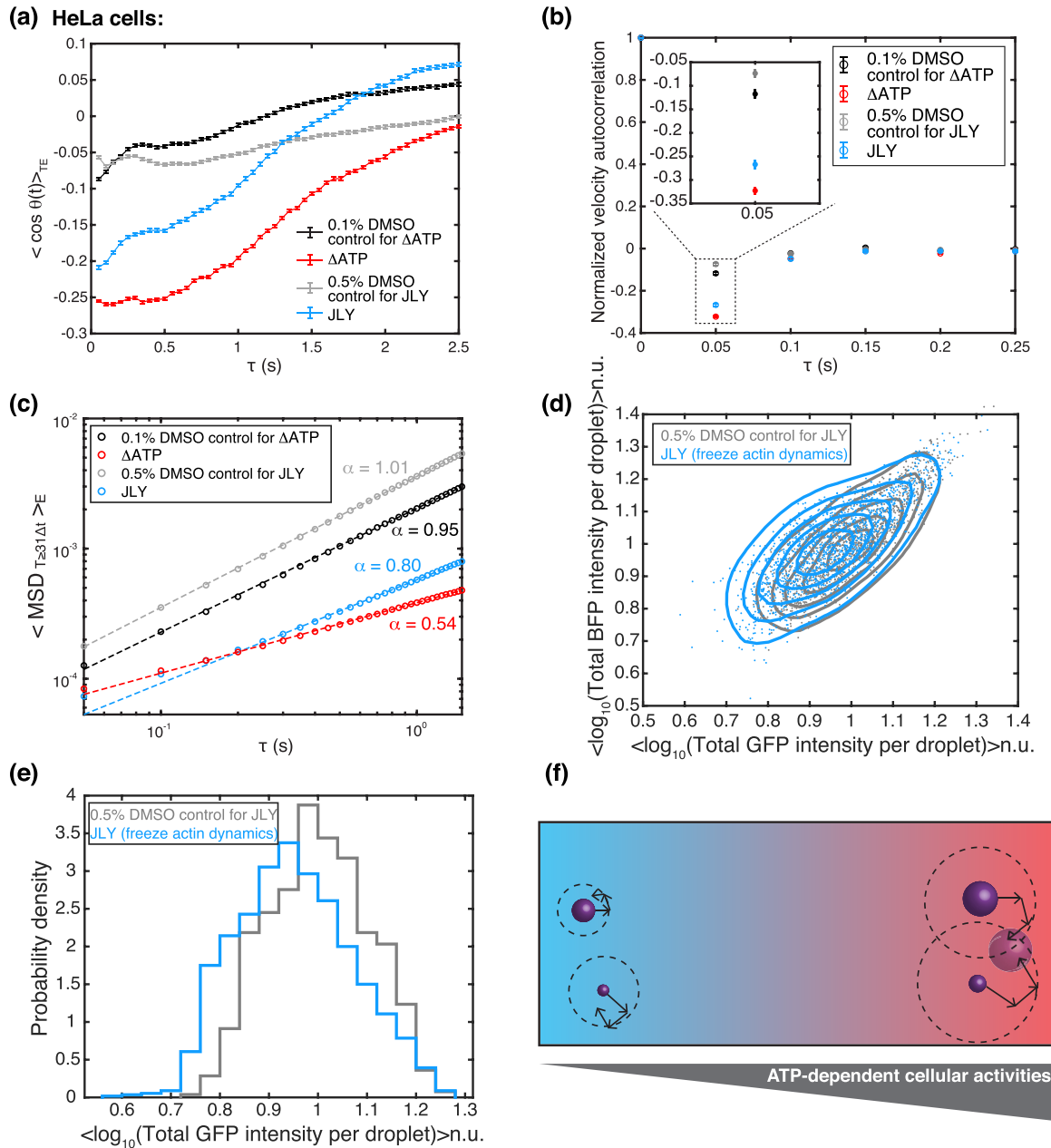


FIG. 7. ATP-dependent cellular activity facilitates droplet growth by promoting long-range cellular structural reorganization. (a) Angle correlation analyses of droplets in mammalian HeLa cells that had preformed after 1 hour of GA induction with DMSO (solvent control) and subsequently treated with 1-hour ATP depletion or 1-hour JLY treatment (to freeze actin dynamics) conditions. (b) Normalized velocity autocorrelation for droplet trajectories in the same conditions as (a). (c) Ensemble-time-averaged MSD analyses of droplet trajectories in the same conditions as (a). (d) Phase diagram of synDrop using total BFP and GFP intensities per droplet, normalized to the median value of droplets in the DMSO control condition. Droplets were induced for 1–2 hours in the presence of solvent control (DMSO) or JLY treatment. (e) Histogram of normalized total GFP intensities per droplet (logarithmic scale) in the same conditions as (d). (f) Model for how ATP-dependent cellular activities may influence droplet growth.

[Fig. 6(c)]. This approach gave similar results in our angular correlation analyses: ATP depletion led to a reduction in the values of the angular correlation function at all timescales, with more prolonged ATP depletion leading to larger reductions [Fig. 6(d)]. Therefore, increased confinement after ATP depletion is not a consequence of differences in synDrop size.

Finally, we used hypo-osmotic shock to investigate whether equalizing droplet diffusivity at short timescales and

length scales between control and ATP-depleted conditions would also equalize confinement. We found similar patterns of confinement after hypo-osmotic shock: Although local diffusivity was equalized [Fig. 4(d)], ATP depletion still led to increased synDrop confinement [Fig. 6(e)] and cytoplasmic elasticity [Fig. 6(f)]. Together, these results are consistent with a model where the rate of droplet growth through coalescence depends on droplet diffusivities over both short and long timescales and length scales. While hypo-osmotic shock

increases droplet local diffusivity at short timescales and length scales, it is ineffective in reversing the increased confinement and elasticity at long timescales and length scales that result from ATP depletion.

We observed similar results in mammalian HeLa cells. Angular correlation values were reduced compared to control after ATP depletion [Fig. 7(a), red line]. Therefore, ATP-dependent activities are required to reduce confinement in mammalian cells. We next inhibited actomyosin dynamics using the inhibitor JLY cocktail. The treatment led to decreased angular correlation values at time lags of less than 1 s, indicating that actomyosin dynamics are required to decrease confinement. However, at time lags of larger than 1.5 s, JLY treatment slightly increased angular correlation values. We hypothesize that this might be due to an imperfect balance in the effects of the three drugs in the JLY cocktail, resulting in a failure to fully arrest actomyosin dynamics at the molecular level. This effect may be minimal at short timescales but can become more significant over longer timescales.

In addition to driving ATP-dependent motion, the cytoskeleton also plays a critical role in determining cellular elasticity [7]. Therefore, we also analyzed velocity autocorrelation before and after ATP depletion or JLY treatment. We found that both treatments led to an increase in the magnitude of the negative peak corresponding to antipersistent particle motion. Thus, either loss of ATP or inhibition of actomyosin dynamics increases the elasticity of the mammalian cytoplasm [Fig. 7(b)], supporting our hypothesis that ATP-dependent cellular activities can modulate long-range rearrangement of cellular structures, leading to less elastic confinement of the intracellular environment.

Confinement within a fixed volume can also result in negative velocity autocorrelation. However, the ensemble-time-averaged mean square displacements (MSDs) did not reach a plateau at longer time lags [Fig. 7(c)], suggesting that the data are not well explained by a fixed boundary confinement. Rather, we observed that data points at longer time lags were fit with a higher exponent α than shorter time lags [Fig. 7(c)]. Control cells had an exponent close to 1, suggesting combined effects of ATP-dependent cellular activities and cytoplasmic elasticity [47], while ATP depletion or freezing actomyosin dynamics with JLY led to a smaller exponent. These results further indicate that ATP-dependent long-range cellular structural rearrangement promotes condensate movement at longer time lags.

Finally, we examined the effect of JLY treatment on droplet formation in HeLa cells. We compared the droplet phase diagram of control cells to that of cells treated with the JLY cocktail at the same time as synDrop induction. We found that droplet intensities were smaller in JLY-treated cells compared to the DMSO control [Figs. 7(d) and 7(e)]. Overall, these results support a model in which the actin cytoskeleton promotes long-range structural rearrangements and thereby reduces elastic confinement in the cytoplasm, enabling droplet growth through coalescence [Fig. 7(f)].

III. DISCUSSION

Membraneless organelles carry out many essential cellular functions within cells [48]. Therefore, it is important

to understand the spatial and temporal information associated with membraneless organelle formation and dissolution. Many studies have focused on specific chemical signals [49], but few studies have looked at physical cues. Here, we demonstrated that intracellular macromolecular crowding and ATP-dependent cellular activity can have dramatic effects on condensate formation. Macromolecular crowding promotes droplet nucleation by reducing effective dissociation constants of binding reactions, but inhibits droplet growth by reducing droplet diffusivities. ATP-dependent cellular activity promotes droplet growth by fluidizing cellular environment through promoting long-range structural rearrangements. Therefore, two of the most unusual properties of the intracellular environment seem to work together to optimize mesoscale assembly.

Macromolecular crowding has several effects on molecular assembly. First, it increases the local concentrations of molecules due to the excluded volume occupied by macromolecular crowders [4]. Second, it imposes depletion-attraction forces that increase the propensity of molecular assembly [3]. The cytoplasmic excluded volume is dominated by mesoscale particles, in particular ribosomes; therefore, this entropic effect is most prominent at the mesoscale. Both effects can affect binding interactions, leading to reduced effective dissociation constants [5]. Crowding agents have been shown to lower the critical concentrations for several *in vitro* reconstituted phase-separation systems [50,51]. However, the inhibition of the kinetics of droplet growth by excess macromolecular crowding is less studied due to the limited availability of controlled *in vivo* phase separation systems.

ATP-dependent cellular activities impart a dynamic and nonequilibrium nature to the intracellular environment, introducing nonthermal forces that amplify random fluctuating motion beyond thermal effects [47]. The cytoskeleton, a key contributor to ATP-dependent activities, exhibits time-dependent material properties [39,52]. On shorter timescales, it behaves as a network of semiflexible polymers primarily influenced by thermal fluctuations, resulting in subdiffusive motion of mesoscale particles. However, on longer timescales, superdiffusive motion is driven by ATP-dependent structural rearrangements [39]. Similar time-dependent material properties have also been observed beyond the context of the cytoskeleton in the mammalian cytoplasm [53] and the membranes of red blood cells [44]. While existing studies on condensates have focused on biochemical aspects of ATP molecules [54] or ATP-consuming processes within condensates [55–57], limited research has investigated the impact of physical properties emerging from environmental ATP-dependent cellular activities on condensate formation.

synDrops have a unique combination of features that make them an ideal platform to investigate how intracellular biophysical environments affect condensates assembly. Their nucleation and growth dynamics can be studied on a reasonable timescale (minutes to 1 hour). In contrast to endogenous condensates, the synDrops components were designed to minimize the probability of specific interactions with endogenous molecules within cells, including ATP-consuming enzymes. Moreover, the well-defined protein structures and network

geometry make synDrops highly amenable to simulation and analysis with graph-theoretical approaches.

Our study highlights how the intracellular environment modulates mesoscale molecular assembly through a combination of macromolecular crowding and cellular active matter. Notably, the intracellular environment is highly heterogeneous in mesoscale diffusivity [58], reflecting local heterogeneity in macromolecular crowding and cellular activity. These physical variations may underlie the distinct behavior of droplet formation within cells compared to the theoretical prediction that droplets should thermodynamically fuse into a single entity. By actively modulating local macromolecular crowding and cellular activity levels, cells could potentially control the formation of endogenous condensates at different locations via biophysical signals. For example, increased cellular activity, such as actin dynamics near the cell cortex, could facilitate endogenous condensate formation, which might in turn contribute to the nucleation and growth of the cytoskeleton network.

We speculate that changes in the biophysical properties of cells could be sensed by their impacts on condensate assembly. Indeed, a synthetic droplet can modulate the rates of kinase reaction in response to changes in macromolecular crowding, demonstrating the feasibility of this idea in cells [59]. On the other hand, the biophysical properties of the cell interior may also change during disease progression, leading to aberrant phase separation of endogenous condensates. Our study provides a framework to guide future investigations into the effects of intracellular biophysical properties on endogenous condensate formation and dissolution and their relevance to normal biology and disease pathology.

IV. MATERIALS AND METHODS

A. Plasmid construction

For yeast plasmids, open reading frames (ORFs) encoding full length Gid and Gai 1–92 [23], dimer (PDB: 4LTB) and hexamer (PDB: 3BEY) [15], green fluorescent protein (Superfolder GFP, PDB: 2B3P), and blue fluorescent protein (mTagBFP, PDB: 3M24) were first amplified using PCR. Using Gibson assembly, we then fused each ORF: Gai-BFP-3BEY and Gid-4LTB-GFP with a strong yeast promoter from TDH3, an N-terminal nuclear export signaling sequence, and a yeast terminator from CYC1, and subsequently assembled into yeast backbone vectors pRS304 and pRS306, respectively. For mammalian plasmids, we codon optimized synDrop ORFs based on codon usage of *Homo sapiens* (Twist bioscience, CA). We then used oligo overhangs to introduce a P2A ribosome-skipping sequence between Gai-BEY-3BEY and Gid-4LTB-GFP, and combined them into a single plasmid driven by the CMV promoter using Gibson assembly. The final plasmid was designed for lentiviral transduction of mammalian cells (based on pLVX backbone, Takara Catalog No. 632159).

B. Yeast transformation

Two plasmids encoding the two components of the yeast synDrop system were first linearized by restriction enzyme digestion within the auxotrophic marker region. The

linearized plasmids were then transformed into W303 yeast strains (*MATa leu2-3, 112 trip1-1 can1-100 ura3-1 ade2-1 his3-11-,15*) sequentially using a LiAc-based protocol [60]. A single yeast cell colony was then selected based on whether condensates were able to form after 1 hour of 300 μ M GA induction.

C. Mammalian cell transient transfection

Mammalian HeLa cells were plated on a six-well plate in high-glucose Dulbecco's Modified Eagle Medium (DMEM) with L-glutamine (Gibco) supplemented with 10% fetal bovine serum (FBS; Gemini Bio), penicillin (100 U/ml), and streptomycin (100 μ g/ml) (Gibco). Cells were incubated at 37 °C with 5% CO₂ in a humidified incubator and grown to approximately 60–80% confluency after one day of plating. On the next day, cells were transiently transfected using 1 μ g of plasmid and 3 μ l of FuGENE HD transfection reagent (Promega) based on manufacturer's protocol. After 24 hours, cells were ready for imaging by replacing with fresh supplemented DMEM. Induction of synDrops in HeLa cells was performed by adding GA till 100 μ M final concentration.

D. Drug treatment

To deplete ATP, *S. cerevisiae* cells were treated with 20 mM 2-deoxyglucose (2-DG) and 10 μ M antimycin A in synthetic complete (SC) media without glucose [61]. The media was further supplemented with either 80 mM sorbitol for isotonic buffer condition or 10 mM sorbitol for hypo-osmotic buffer condition. Additionally, the pH was balanced to 7.5 using a 50 mM Tris-HCl buffer. For ATP depletion in mammalian HeLa cells, a mixture of 6 mM 2-DG and 1 μ M carbonyl cyanide-trifluoromethoxy phenylhydrazone (FCCP) in CO₂-independent medium supplemented with L-glutamine was added to cells for 1 hour [62].

To inhibit TOC1 signaling, *S. cerevisiae* cells were treated with 1 μ M rapamycin for 2 hours in SCD media [2]. For JLY treatment, mammalian HeLa cells were first treated with 10 μ M y27632 for 10 min, followed by the addition of jasplakinolide and latrunculin B to final concentrations of 10 μ M y27532, 8 μ M jasplakinolide, and 5 μ M latrunculin B [40] for 1 hour in CO₂-independent medium supplemented with L-glutamine.

E. Microscope imaging of yeast cells

Yeast cells were imaged using a Nikon TI Eclipse microscope with a 100 \times oil objective (100 \times phase, NA = 1.4, part no. MRD31901) and a sCMOS camera (Zyla, Andor, part no. ZYLA-4.2p-CL10). An epifluorescence LED light source (Spectra X, part no. 77074160) was used for imaging yeast cells with synDrops. The GFP channel was imaged through a GFP filter set (EF-EGFP (FITC/Cy2), Chroma, part no. 49002), while the BFP channel was imaged through a quad-band filter set (ET – 405/488/561/640 nm, Chroma, part no. TRF89901). Z stacks were taken every minute for the first 10 min and every 5 min thereafter following synDrop induction, for each channel, with an interval of 0.5 μ m and total distance of 3 μ m (seven slices). Average projections of Z stacks were used for subsequent imaging analyses. Movies for

tracking synDrop motion were also recorded using the GFP channel, but with a 50-ms frame rate without delay (20 Hz) for a total of 20 s (total 400 frames).

For microrheology, we used 40-nm-diameter genetically encoded multimeric nanoparticles (GEMs). To record GEM movement, we used highly inclined thin illumination (HILO) microscopy. Each GEM movie was imaged on a single focal plane at 10-ms frame rate with no delay (100 Hz) for a total of 4 s (total 400 frames) using a 488-nm laser light source at 100% power (OBIS 100 mW LX 488 nm, Coherent, part no. 1236444) and with a GFP filter set (EF-EGFP (FITC/Cy2), Chroma, part no. 49002).

F. Microscope imaging of mammalian cells

Mammalian cells with synDrops were imaged using a confocal Nikon TI Eclipse microscope with a spinning disk unit (CSU-X1 spinning disk, Yokogawa, part no. 99459), with a 60 \times oil objective (60 \times , NA = 1.49, part no. MRD01691) and a sCMOS camera (Prime 95B, Teledyne Photometrics). The GFP channel was excited using a laser light source (OBIS 100 mW LX 488 nm, Coherent, part no. 1236444) and imaged through a GFP emission filter (EF525/36m, Chroma, part no. 77014803). The BFP channel was excited using an LED light source (X-Cite 120LED, Excelitas, part no. 010-00326R) and imaged through a DAPI filter set (ET-DAPI, Chroma, part no. 49028). Z stacks were taken after 1 hour of GA induction for each channel with an interval of 0.5 μ m and total distance of 6 μ m (13 slices). Average projections of Z stacks were used for subsequent imaging analyses. Droplet movies were also recorded using the GFP channel with 50-ms frame rate without delay (20 Hz) for a total of 20 s (total 400 frames).

G. Image analyses

To characterize the properties of synDrops within cells, Z projections were analyzed using the Trackmate plugin [63] on ImageJ [64,65]. Due to higher signal-to-noise ratio in the GFP channel, droplets were detected using the GFP channel unless otherwise stated. We applied a LoG (Laplacian of Gaussian filter) detector on Trackmate to identify the droplets, with 1 μ m “estimated object diameter” and a fixed “quality threshold” across all different conditions in each experiment. To determine the total intensity per droplet, we defined a circle that was larger than the droplet, computed the mean pixel intensity within this identified region, and then subtracted the background mean pixel intensity. This measurement is proportional to the total number of fluorescent molecules within a droplet. Results of particle detection from Trackmate included all time points and were then saved as *xlm* files. Using home-written MATLAB (2019a) code, we subsequently extracted and compiled properties of the droplets, including raw mean pixel intensities and their locations in the images. We also determined the background mean pixel intensity by randomly selecting 20 circles with the same 1- μ m diameter in each image from areas away from droplets. YeastSpotter [66] was used to identify single yeast cells, which generated ImageJ mask files indicating locations of each individual yeast cell. By combining with position information of droplets, we

computed the number of droplets per cell using home-written MATLAB code.

To obtain droplet diffusivities, we used simple linear assignment problem (LAP) particle tracking function on Trackmate in addition to particle detection, with maximal linking and gap-closing distance of 390 nm and maximal gap-closing frame interval of 1. Only trajectories with more than 10 time points were included for subsequent mean squared displacement analyses using home-written MATLAB code.

To determine GEM diffusivities, GEM trajectories were detected using the Mosaic plugin [67] on ImageJ [64,65] with particle detection parameters of radius 3, cutoff 0, per/Abs (percentile) 0.1, and particle linking parameters of link range 1, displacement 5 with Brownian dynamics. We only selected trajectories with more than 10 time points for subsequent mean squared displacement analyses using home-written MATLAB code.

To generate density plots based on the scattered data points, the data space was separated into 25 \times 25 different regions based on the minimum and maximum values on both *x* and *y* axes. By counting the number of data points within each region, two-dimensional (2D) density matrices were generated and smoothed using the MATLAB function `scattercloud` [68]. The contour lines were further obtained using MATLAB function `contour`.

H. MD simulation analyses

We used graph-theory-based methods for analyzing MD simulations. Each molecule in our MD simulations had a unique number identifier and was treated as the node for the graph. Bonds formed at each time point were recorded based on molecule pairs that formed each bond, and were treated as the edges for the graph. The graph at each time point was then constructed by providing both node and edge information inputs using the `igraph` [69] package in PYTHON. To identify clusters, a distance matrix was first calculated based on the topological shortest path that links each pair of molecules. Subsequently, a hierarchical clustering algorithm was employed on the distance matrix. This led to the reordering of molecule sequences, with molecules within each cluster being grouped together. Cluster size was then determined based on the number of molecules that were within each cluster. Locations of each molecule were also recorded at each time point.

To calculate cluster diffusivity, clusters with size larger than 10 molecules were first identified at each time point. Pairwise clusters from consecutive time points were connected from the last time point by determining the largest number of same nodes, thus forming trajectories. If a cluster's size changed by 20 within a time interval, it was considered as a new cluster and tracked as a distinct trajectory. Only trajectories with more than 10 time points were selected for calculating cluster diffusivities, where mean squared displacement of the cluster's center of mass for each trajectory was fitted over the first 10 time intervals. All analyses were performed using home-written PYTHON3 code.

To determine the effective dissociation constants (K_d) of the chemical bonds, we analyzed the kinetics of bond formation in monovalent MD simulations until equilibrium was achieved. In this monovalent system (where the dimers and

hexamers are in a 1:1 stoichiometric ratio), we reduced the available binding sites of two components from six and two to one and one each. By fitting the data to an inverse exponential decay function, we extracted the number of bonds formed at equilibrium. Subsequently, K_d was calculated based on the concentration of all species at equilibrium, using the formula for a dimerization reaction $A + B \leftrightarrow AB$,

$$K_d = \frac{[A][B]}{[AB]} = \frac{N_A N_B}{N_{AB} V},$$

where V is the volume of the simulation box.

To roughly match simulation timescales to experimental ones, the mean squared displacement of 40-nm GEM particles in simulations using our HOOMD-blue model were fit to the Einstein diffusion relation in 3D: $MSD(t) = 6Dt$ for long times, and D was obtained in units of $\mu\text{m}^2/\tau$. The unit of time $\tau = 7.5 \times 10^{-8}$ s was then obtained by matching this D to an approximate cellular value of $0.3 \mu\text{m}^2/\text{s}$ [2].

I. Simulations set up using HOOMD-blue

An agent-based MD simulation approach has been developed to study the synDrops system. MD simulations were performed using HOOMD-blue v2.9.6 [25,26], making use of a single graphics processing unit (GPU) to achieve considerable acceleration in simulation speeds. We use coarse-grained (CG) representations of each synDrops component: (i) a sphere with six rigid evenly distributed binding sites to represent the hexamer and (ii) three spheres in a rodlike arrangement with two complementary binding sites at two ends to represent the rigid coiled-coil dimer. We have 1170 dimers and 390 hexamers within a cubic box with 860-nm sides (maintaining a 3:1 stoichiometric ratio of dimers and hexamers to have a 1:1 ratio of complementary binding sites). This results in concentrations of $3 \mu\text{M}$ for dimers and $1 \mu\text{M}$ for hexamers, similar to our estimated values in experiment. Finally, 20 spheres of diameter 40 nm are added to mimic the trace particles: GEMs in the experiment.

In addition, spherical components of various sizes without any binding site are added in the system to mimic the crowded cellular environment. For the initial configuration, the CG components are arranged in a lattice whose positions are generated from a CsCl-type lattice generator using the “lattice” module from the ASE (Atomic Simulation Environment) [70] package. We ran MD simulations with varying volume fractions of ribosomes to study the effect of crowding in synDrops assembly. We also varied the effective temperatures that only govern the ribosome movements to study how cellular activities affect synDrops assembly.

Binding occurs through complementary interaction sites between dimers and hexamers. We modeled such covalent interactions by developing an open-source C++ plugin, called the Dynamic Bond Updater [27], in HOOMD-blue that builds upon a model for epoxy binding developed in Ref. [71]. The Bond Updater, for every n steps during the MD simulation, stochastically adds or removes dynamic bonds. Binding events occur with a fixed probability P_{on} at a critical distance d_{bind} between interaction sites, while unbinding events occur with a probability P_{off} . Using our dynamic bonding frame-

work, we thus have controls over our binding and unbinding rate constants k_{on} and k_{off} , respectively; the bond affinity ε is defined by

$$\Delta G = k_B T \ln(k_{\text{on}}/k_{\text{off}}) \equiv \varepsilon$$

and can be increased by lowering the unbinding rate constant k_{off} . We ensure that the dynamic bonding model satisfies detailed balance using a particular Metropolis-like criterion [72–74], so that the system moves towards an equilibrium ensemble as bonds form and dissolve dynamically. We use the cell neighbor list [75] to accelerate nonbonded agents’ calculations and possible bonding pairs’ constructions.

Interactions between crowdiers and synDrops proteins occur via a soft repulsion potential [27] defined by

$$U_{\text{soft}}(r) = \varepsilon_{\text{soft}} (1 - (r/r_{\text{cut}})^4) \quad \text{if } r < r_{\text{cut}} \text{ and} \\ U_{\text{soft}}(r) = 0 \quad \text{if } r \geq r_{\text{cut}},$$

where smoothing was applied using HOOMD-blue’s XPLORE [26] smoothing function. The soft potential was implemented by using HOOMD-blue’s tabulated potential option (with 1000 interpolation points between $r_{\text{min}} = 0$ and $r_{\text{max}} = 1.5\sigma$, where σ is the sum of the radii of the particles). Here, r_{on} is chosen as the point at which the smoothing starts. We set $r_{\text{on}} = 0.95r_{\text{cut}}$ for our simulations, and $r_{\text{cut}} = \sigma$. There is no soft repulsion between complementary binding interaction sites on hexamers and dimers, where we implemented a Lennard-Jones (LJ) [76–79] attraction between the hexamer and dimer rigid bodies, with a cutoff distance equal to 2.5σ . All objects in the system undergo thermal fluctuations using Langevin [80] dynamics, with drag forces proportional to the diameter. The dimensions of every CG component approximate their respective crystal structures. Within our MD simulations, we typically use periodic boundary conditions (PBCs). However, we also have the option of adding “walls” to confine our system in a “closed box.” For volume fractions up to 35%, we are able to place ribosomes in the box without overlaps through random sequential insertion. For higher concentrations, we first set up an initial simulation box size using lengths of 1400 nm on a side (4.3 times the target volume) and the appropriate number of ribosomes, and then compress the system to the target size of 860 nm linearly over 5×10^5 simulation steps (using the “hoomd.variant” module of HOOMD-blue), and finally turn on dynamic bonding in the system to record synDrops dynamics.

To study how nonthermal cellular activity [41,42] impacts formation of synDrops via MD simulations, we assign the crowdiers a different effective temperature T_c from the rest of the system, which can be achieved through separate Langevin “thermostats” in HOOMD-blue. We ran a different set of MD simulations at a fixed volume fraction of ribosomes (= 30%) but varying the crowder effective temperatures T_c .

J. Simulations set up using custom-developed JAVA program

A custom three-dimensional agent-based JAVA program was developed to simulate aggregation and cluster formations of proteins in a cellular environment. All objects in these simulations are spheres, or spherical aggregates, that move in space as a result of applied forces. These forces arise in three distinct ways: through collisions with other spheres and

with the boundaries of the simulation, through bonds to other spheres, and through a random force and torque applied to approximate the Brownian motion of each object. The movements of all molecules then follow Langevin dynamics with a defined effective temperature.

Collisions are resolved with a simple rule: at a low Reynolds number we can calculate the exact force to resolve any pairwise collision. This method is described in detail in Ref. [81]. All the pairwise forces are summed and then attenuated for numerical stability such that collisions resolve over several time steps (not instantaneously). Translational bond forces are resolved in the same way: by calculating the force required to bring a stretched bond back to its relaxed position. By contrast, torques are calculated with a linear torsional spring. Brownian forces and torques are randomly taken from a Gaussian distribution with a mean of zero and variance of $2D\Delta t$, where D is the diffusivity of the object (which can differ in all three translational and rotational degrees of freedom) and Δt the time step.

The two protein components of the synDrops system were modeled as spheres having six or two uniformly distributed binding sites on their surface [extended data, Fig. 1(c)]. The size of each sphere was determined based on its experimental correspondence with known protein crystal structures. Bond kinetics in the model arise by prescribing binding and unbinding rates, with binding occurring between available sites only when they are within a minimum distance of each other. The unbinding rate is assumed to be independent of any strain in the bond. After selecting appropriate values for minimum binding distance and unbinding rate, we ensured that the dissociation constant for the chemical bond ranged between 1 and 10 μM . As in the HOOMD-blue system, we use 1170 dimers, 390 hexamers, and varying numbers of ribosomes in a box with side length 860 nm.

ACKNOWLEDGMENTS

We thank Dajun Sang and Wells Burrell for their assistance in engineering protein constructs. We thank Meta Heidenreich for helpful discussions. L.J.H. and T.S. were funded by National Institutes of Health (NIH) Awards No. R01 GM132447 and No. R37 CA240765, the American Cancer Society Cornelia T Bailey Research Award, the NIH Director's Transformative Research Award No. TR01 NS127186, the Air Force Office of Scientific Research (AFoSR FA9550-21-1-3503 0091), and the Human Frontier Science Program (RGP0016/2022-102). G.M.H. and G.M. were supported by the NIH via Award No. R35-GM138312. This work was supported in part through the NYU IT High Performance Computing resources, services, and staff expertise, and simulations were partially executed on resources supported by the Simons Center for Computational Physical Chemistry at NYU (Simons Foundation Grant No. 839534).

APPENDIX A: RESULTS OBTAINED FROM MODELING SYNDROPS USING AN ALTERNATIVE AGENT-BASED MD SIMULATION PLATFORM

To ensure the generality of conclusions drawn from MD simulations, we developed an alternative agent-based simulation platform using a separate JAVA program. In this simulation, the two protein components of synDrops, hexamer and dimer, are represented as spheres, with six and two binding sites, respectively, with dimensions corresponding to their crystal structures [Fig. 8(a)]. Dynamic interaction occurs between the binding sites on the hexamer and dimer, and is defined by an unbinding probability and a minimum binding distance to initiate binding. Additionally, a third sphere without any binding site was included mimicking ribosomes as macromolecular crowders [Fig. 8(a)]. This

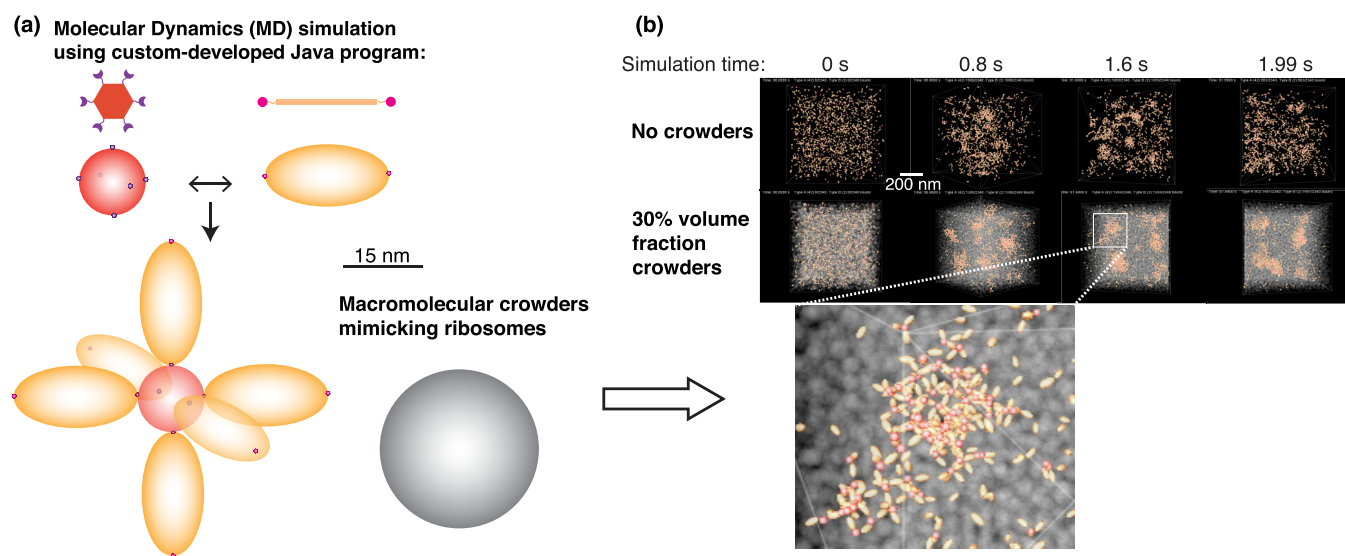


FIG. 8. synDrops modeled in alternative agent-based MD simulation platform. (a) A second MD simulation platform was developed based on a custom JAVA program. The two protein components of the synDrops system were modeled as spheres with either six or two binding sites. The simulation system also includes a third molecular component, without binding sites, that mimics ribosomes as macromolecular crowders. (b) MD simulations of synDrop assembly over time without crowders (top) and with 30% volume fraction of crowders (bottom). The zoomed-in image under 30% volume fraction condition shows the formation of a large cluster.

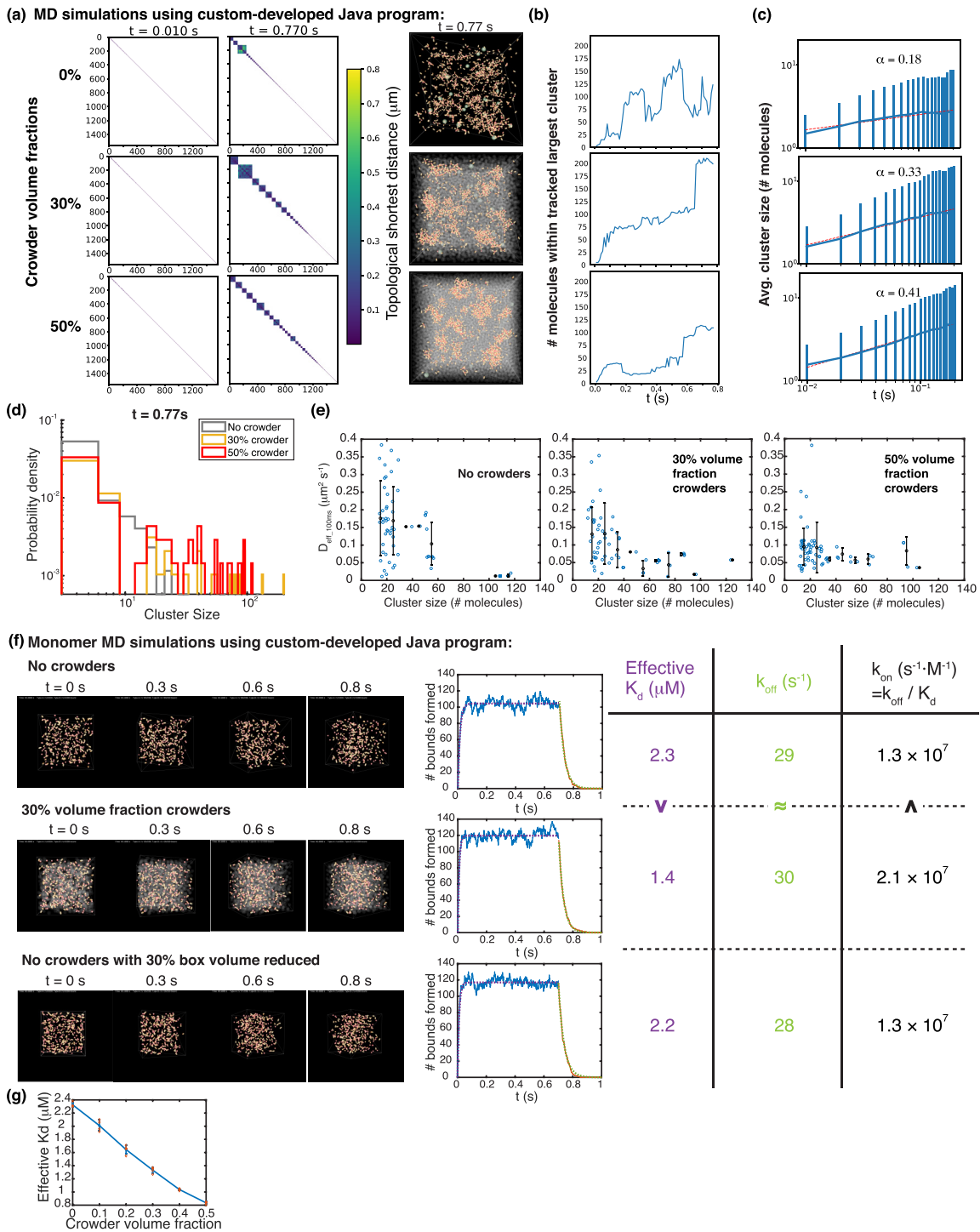


FIG. 9. Simulation results from JAVA-based MD simulations: Increasing molecular crowding promotes synDrop nucleation but inhibits mesoscale growth. [(a)–(e)] Analyses of MD simulations with 0%, 30%, and 50% volume fraction of crowder: (a) Left: Clustergrams representing molecular connectivity, determined by graph theory. Squares on the diagonal are indicative of clusters of molecules. Analyses are shown after 0.01 and 0.77 s simulation time. Right: images of the simulation renderings after 0.77 s. (b) Number of molecules within the largest cluster as a function of time. (c) Average cluster size (number of molecules) as a function of time. Dashed line is the power-law fit for the initial 0.2 s with fitted exponent labeled as α . Error bars are standard deviation (SD). (d) Distribution of cluster sizes (number of molecules) at $t = 0.77$ s. (e) Average cluster diffusivity versus cluster size (number of molecules). Error bars are SD. (f) Monomer MD simulations to determine binding rates. Each protein component was modified to be monovalent and simulations were performed with no crowders (top), 30% volume fraction of crowders (middle), and no crowders but with a 30% reduction in container volume (bottom). After 0.7 s, the binding probability was set to zero, allowing determination of unbinding rates. Effective binding rates (k_{on}), unbinding rates (k_{off}), and dissociation constants (K_d) were inferred from the number of bonds formed over time (table, right). (g) Effective dissociation constants (K_d) as a function of crowder volume fractions. Error bars are SD from three repeats.

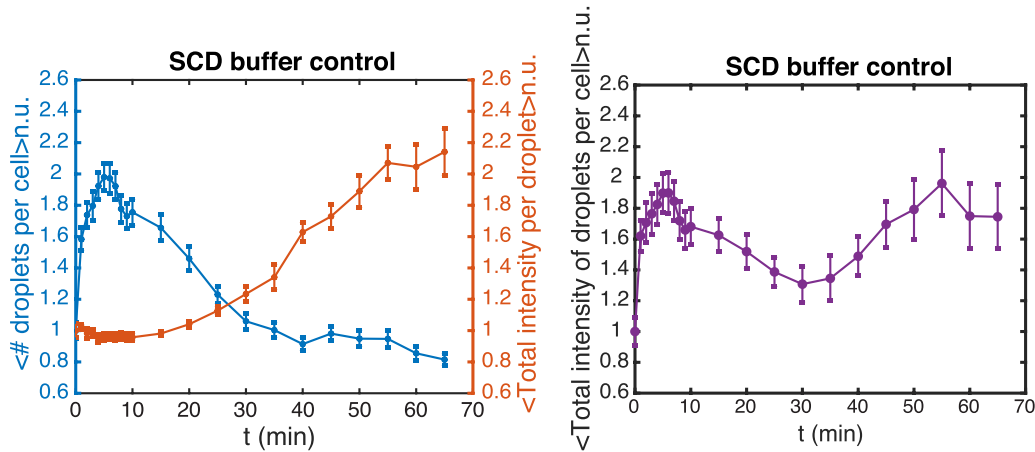


FIG. 10. Kinetics of droplet intensities after synDrop induction in *hog1Δ S. cerevisiae* yeast cells in control conditions. Left: Average number of droplets per cell and average total intensity per droplet, both normalized to their mean values at 0 min, were quantified for 1 hour after synDrop induction with GA in *hog1Δ S. cerevisiae* cells. Error bars are SEM. Right: Normalized total intensity of all droplets per cell, calculated by multiplying the two quantities shown on the left. Error bars are propagated SEM.

simulation platform allows the study of synDrop formation under various conditions [Fig. 8(b)].

To study the impact of macromolecular crowding on synDrops, we simulated synDrop formation under varying volume fractions of crowders. Consistent with the results obtained using the HOOMD-blue engine (Fig. 3), we observed a greater formation of larger clusters under the 30% volume fraction compared to the no-crowder condition. However, as the crowder volume fraction increased to 50%, cluster size became smaller, as revealed by graph-theory-based analyses [Fig. 9(a)], tracking the number of molecules within the largest cluster [Fig. 9(b)], and assessing the cluster size distribution at the final time point of simulations [Fig. 9(d)]. We then focused on the nucleation process by quantifying the initial growth rate of the averaged cluster size. Notably, we found that increasing crowder volume fraction monotonically increased the initial growth rate, suggesting that macromolecular crowding promotes synDrop nucleation [Fig. 9(c)].

However, cluster diffusivity analyses revealed a monotonic decrease when increasing macromolecular crowding, consistent with a model where crowding inhibits the growth of synDrops by coalescence [Fig. 9(e)].

To investigate the molecular mechanisms of how macromolecular crowding promotes synDrop nucleation, we simulated a simplified monomer system, where each protein component had only one binding site, under different crowder volume fractions [Fig. 9(f)]. Our findings revealed a consistent reduction in effective dissociation constants as crowder volume fractions increased [Fig. 9(g)], indicating that binding is favored under increased macromolecular crowding conditions in our MD simulations.

APPENDIX B: SYNDROPS MAINLY GROW THROUGH DROPLET COALESCENCE

To assess if synDrop growth mainly occurs through droplet coalescence, we examined the kinetics of droplet intensities

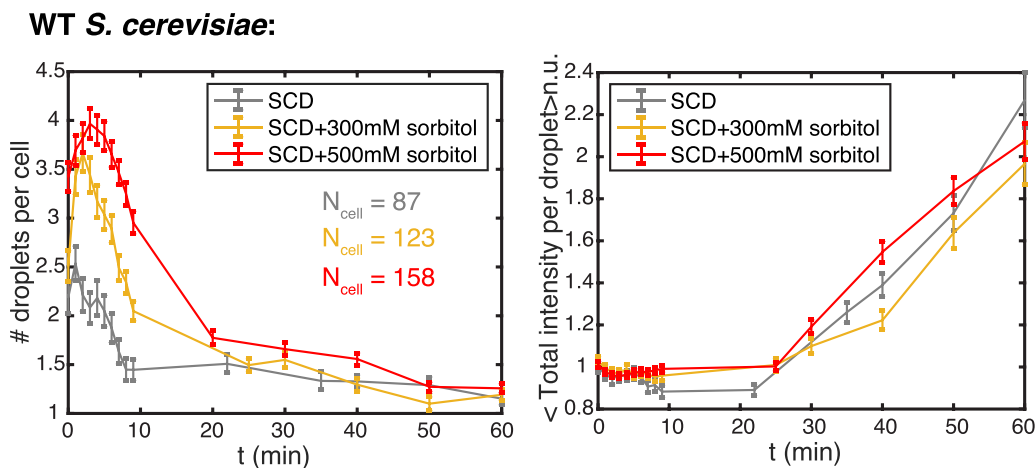


FIG. 11. Kinetics of synDrop formation in WT *S. cerevisiae* yeast cells. Average number of droplets per cell (left) and normalized total intensity per droplet (right) during 1 hour of synDrop induction in WT *S. cerevisiae* yeast cells comparing control conditions to osmotic compression with 300 or 500 mM sorbitol.

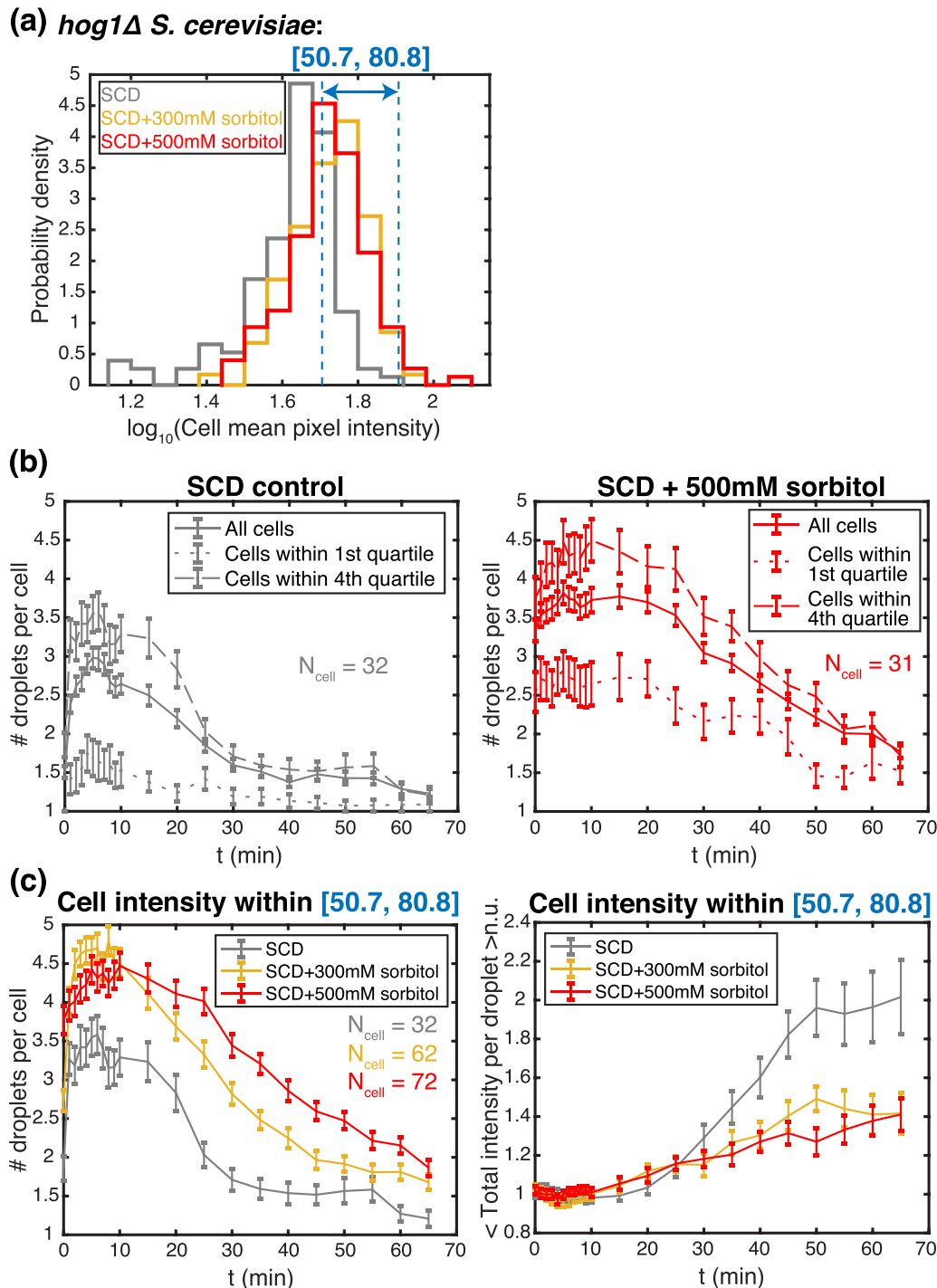


FIG. 12. Dissecting the effects of protein concentration and macromolecular crowding after osmotic compression. (a) Osmotic compression increases protein concentrations, but this effect can be accounted for through selection of a subset of cells. Distributions of GFP intensities (mean pixel fluorescence intensities) of *hog1Δ S. cerevisiae* yeast cells, comparing control to osmotic compression conditions. The fourth quartile of GFP intensities in control conditions is labeled by blue dashed lines. (b) Average number of droplets per *hog1Δ S. cerevisiae* cell after synDrop induction in control (left) and osmotic compression (500 mM sorbitol, right) conditions, comparing all cells, cells with GFP intensities in the lowest (first) quartile, and cells with GFP intensities in the highest (fourth) quartile. Error bars are SEM. (c) Kinetics of formation of synDrops in cells with GFP intensities in the fourth quartile of control conditions [blue dashed lines in (a)] comparing control to osmotic compression (300 or 500 mM sorbitol) conditions. Error bars are SEM.

after synDrop induction in control conditions. We first normalized the average number of droplets per cell and total intensity per droplet relative to their values at 0 min (Fig. 10,

left). Subsequently, we calculated the normalized total intensity of all droplets per cell by multiplying the normalized total intensity per droplet by the normalized number of

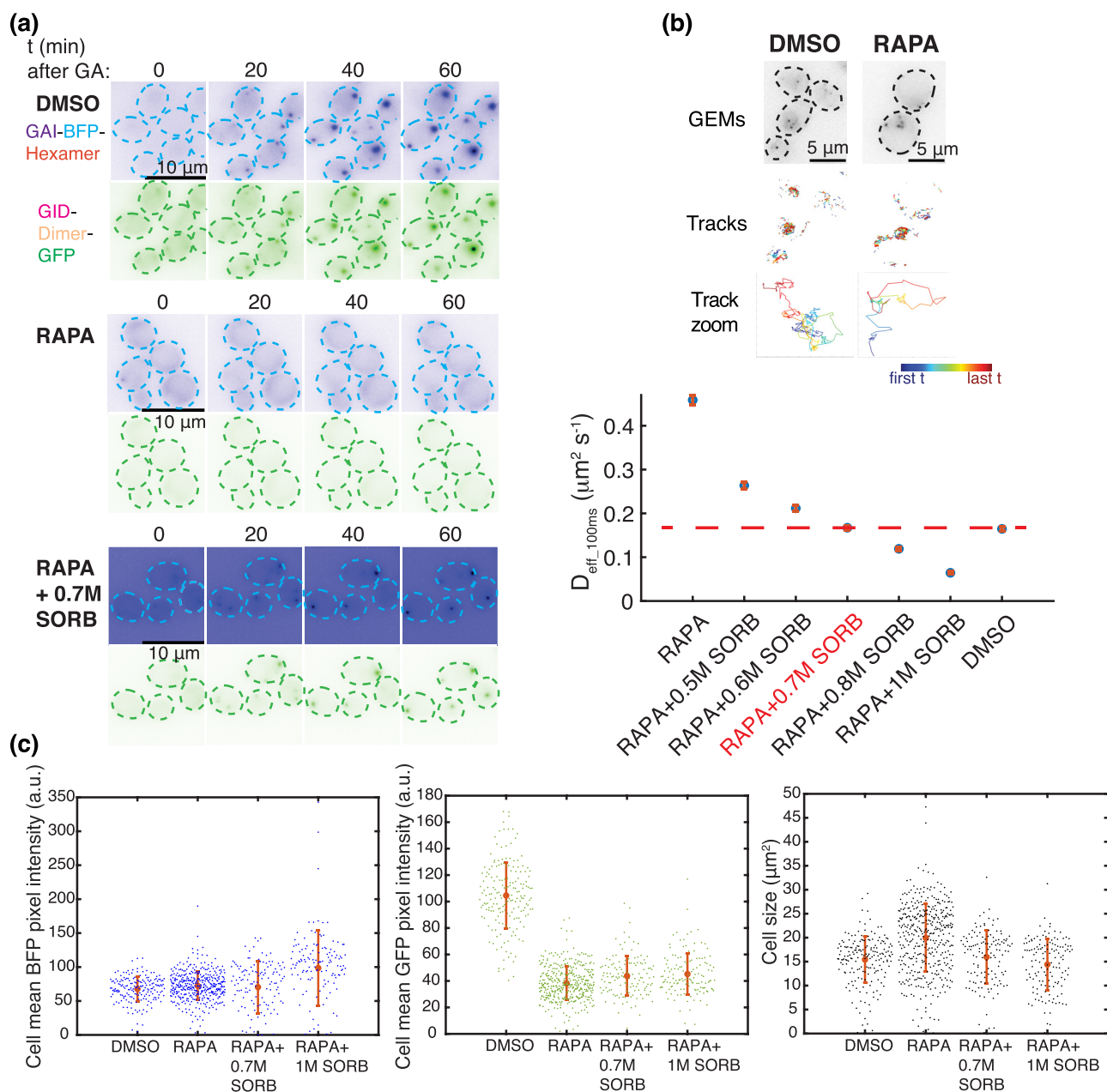


FIG. 13. Dissecting the effects of protein concentration and macromolecular crowding after rapamycin treatment. (a) Representative images of synDrops during 1 hour after synDrop induction with GA comparing *hog1Δ S. cerevisiae* yeast cells treated with DMSO (control), rapamycin pretreatment for 2 hours (RAPA), and rapamycin pretreatment for 2 hours followed by osmotic compression to restore genetically encoded multimeric (GEM) nanoparticle diffusivity to control values (RAPA + 0.7 M Sorb). (b) GEM nanoparticles were used to determine the sorbitol concentration that restores mesoscale crowding in cells pretreated with RAPA for 2 hours to a level comparable to DMSO control cells. (c) Quantifications of cell mean BFP (left) and GFP (middle) pixel intensities, and cell size (right) comparing *hog1Δ S. cerevisiae* yeast cells treated with DMSO control; RAPA; RAPA followed by 0.7 M sorbitol; and RAPA followed by 1 M sorbitol. Error bars are SD.

droplets per cell (Fig. 10, right). As droplets nucleated and formed in the first 10 min, we observed an increase in the normalized total intensities of droplets per cell. However, after 10 min, these values remained relatively constant, fluctuating around 1.6, thus supporting the notion of droplets mainly growing through coalescence.

APPENDIX C: DISSECTING THE EFFECTS OF PROTEIN CONCENTRATION AND MACROMOLECULAR CROWDING AFTER OSMOTIC COMPRESSION

Wild-type (WT) *S. cerevisiae* yeast cells can quickly adapt to osmotic compression by producing glycerol as an osmolyte to restore their volume [30]. In the mild osmotic

compression conditions of our experiments, this adaptation can occur within 15–30 min. When observing synDrop formation kinetics in WT yeast cells, we noted an increase in the number of droplets per cell in the initial 10 min under osmotically compressed conditions compared to control (Fig. 11, left), suggesting enhanced nucleation upon increased molecular crowding. However, the growth curves of total intensity per droplet were indistinguishable after 20 min (Fig. 11, right), indicating the onset of osmo-adaptation, which restores normal macromolecular crowding levels.

To circumvent the effect of osmo-adaptation in WT yeast cells, we used *hog1Δ* yeast cells. Hog1p is a key regulatory kinase, required for rapid glycerol accumulation after osmotic shock [30]. Deletion of the *HOG1* gene greatly diminishes this osmo-adaptation mechanism.

Osmotically compressing *hog1Δ* yeast cells leads to decreased cell sizes, which increases both macromolecular crowding and the concentration of synDrop protein components. As condensate formation can be affected by both molecular crowding and component concentrations, our next objective was to dissect the relative impact of these two factors on synDrop formation after osmotic compression. To achieve this, we first quantified the overall protein concentration changes within individual yeast cells under both control and osmotically compressed conditions [Fig. 12(a)]. Indeed, overall protein concentrations increased under osmotic compressed conditions. To account for this factor, we leveraged the intrinsic variations in protein concentrations within each condition by selectively choosing cells with protein fluorescence intensities in either the lowest quartile (first) or highest quartile (fourth). We found that cells with higher protein concentrations indeed exhibited a higher number of droplets compared to cells with lower protein concentrations [Fig. 12(b)]. These effects were qualitatively consistent for both control and osmotic compression conditions. These results suggest that protein concentrations indeed impact synDrop formation kinetics.

To remove the potential confounding effects of changes in protein concentration, we next selected the subset of cells from control and osmotically compressed conditions that were within a similar intensity range [Fig. 12(a), blue dotted lines]. Analyzing these cells, we found that droplet nucleation was promoted and growth was inhibited after osmotic compression [Fig. 12(c)] and these results were quantitatively very similar to the full data set [Figs. 2(a) and 2(b)]. Together these results suggest that increased macromolecular crowding is the main factor impacting synDrop formation kinetics after osmotic compression.

APPENDIX D: DISSECTING THE EFFECTS OF PROTEIN CONCENTRATION AND MACROMOLECULAR CROWDING AFTER RAPAMYCIN TREATMENT

Rapamycin treatment lowers macromolecular crowding in yeast cells by inhibiting the TORC pathway, leading to reduced ribosome concentrations [2]. synDrop formation was significantly diminished after rapamycin treatment [Fig. 13(a)]. However, rapamycin treatment not only affects crowding but also inhibits translation and therefore decreases protein concentrations, as indicated by decreased fluorescence intensities, especially of the GFP-labeled dimer component [Fig. 13(c)]. To isolate the effects of macromolecular crowding from protein concentration changes, we used osmotic compression to restore crowding in rapamycin-treated yeast cells. We determined the appropriate sorbitol concentration to restore normal macromolecular crowding using a microrheology approach. In brief, macromolecular crowding can be inferred based on the diffusivity of tracer particles. We used 40-nm-diameter genetically encoded multimeric nanoparticles (40-nm GEMs) as our tracer particles, as they are an appropriate length scale to report on crowding by ribosomes. We titrated sorbitol concentrations in the media until the diffusivity of 40-nm GEMs in rapamycin-treated cells

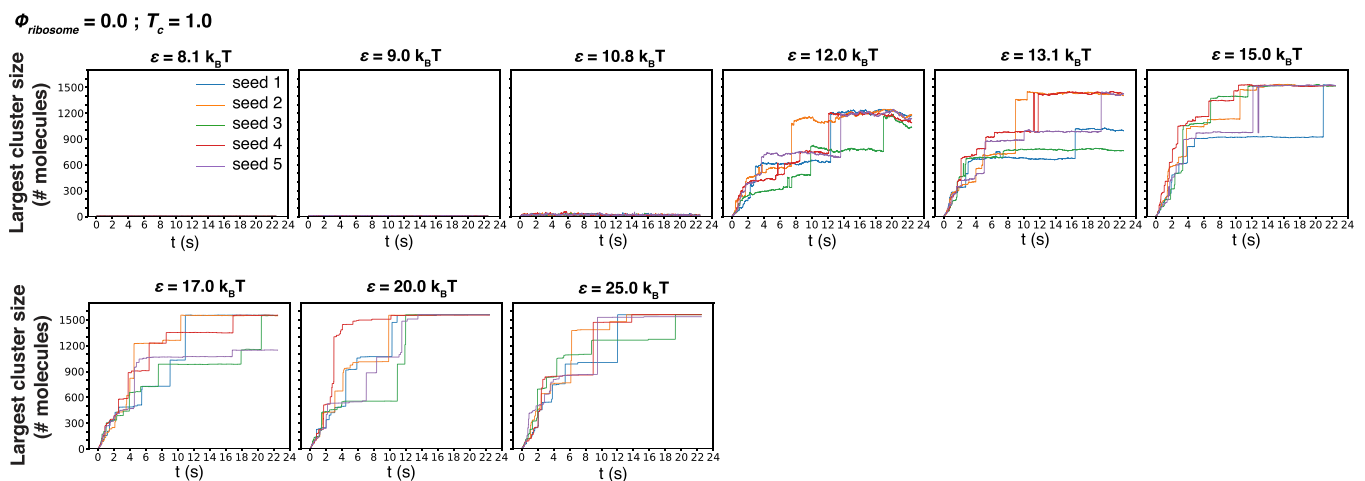


FIG. 14. Largest cluster size over time under conditions with different binding affinities ϵ at 0% crowder and room temperature. Number of molecules within the largest cluster over time in MD simulations using HOOMD-blue, varying the binding affinities between two synDrop components. All simulation conditions are identical to those in Fig. 3(b), with 0% crowders and conducted at room temperature. For each condition, five replicates were simulated, labeled as “seed” from seed 1 to seed 5.

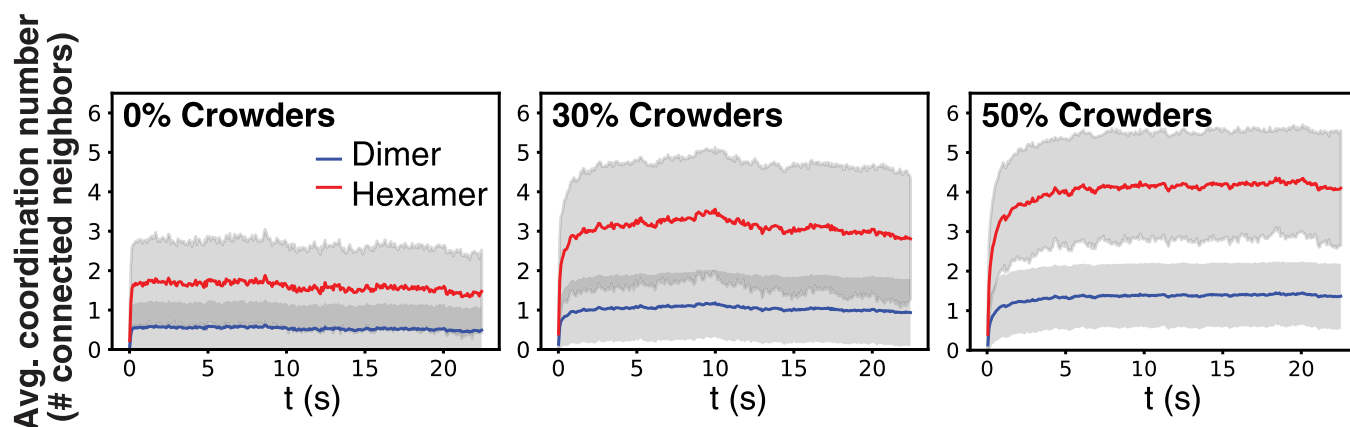


FIG. 15. Average coordination number of dimer and hexamer components under different crowding conditions in MD simulations. Average coordination number (number of directly connected neighbors) for all dimers and hexamers over time under conditions of 0%, 30%, and 50% volume fraction of crowders using the HOOMD-blue simulation model. Gray regions represent standard deviation (SD).

matched that in control (DMSO-treated) cells [Fig. 13(b)]. This approach determined that addition of 0.7 M sorbitol approximately restored normal crowding to rapamycin-treated cells. This osmotic compression only led to a small increase in protein concentration compared to cells treated only with rapamycin [Fig. 13(c)]. Thus, we could dissect the relative effects of changes in macromolecular crowding from the effects of decreased protein concentration. Quantification of synDrop formation in cells treated with rapamycin and 0.7 M sorbitol revealed that synDrop formation was largely recovered [Fig. 13(a); quantified in Figs. 2(c) and 2(d)], suggesting that decreased macromolecular crowding is the main reason for decreased synDrop formation after rapamycin treatment.

APPENDIX E: ADDITIONAL ANALYSES OF MD SIMULATIONS USING HOOMD-BLUE

We varied binding affinities from $8.1k_B T$ to $25.0k_B T$ (Fig. 14) to determine thresholds at which cluster formation would become favorable. Five replicates were included for each condition. The concentrations of dimers and hexamers remained at 3 and 1 μM in all conditions. Reactions were at room temperature, and no crowder was present.

We next examined the changes in averaged coordination number (or number of directly connected neighbors) of dimers and hexamers over time under different crowding conditions: 0%, 30%, and 50% volume fractions of crowders (Fig. 15). We observed that the averaged coordination numbers for both dimers and hexamers increased with crowding.

- [1] J. van den Berg, A. J. Boersma, and B. Poolman, Microorganisms maintain crowding homeostasis, *Nat. Rev. Microbiol.* **15**, 309 (2017).
- [2] M. Delarue *et al.*, mTORC1 controls phase separation and the biophysical properties of the cytoplasm by tuning crowding, *Cell* **174**, 338 (2018).
- [3] S. Asakura and F. Oosawa, Interaction between particles suspended in solutions of macromolecules, *J. Polym. Sci.* **33**, 183 (1958).
- [4] R. J. Ellis, Macromolecular crowding: Obvious but underappreciated, *Trends Biochem. Sci.* **26**, 597 (2001).
- [5] H.-X. Zhou, G. Rivas, and A. P. Minton, Macromolecular crowding and confinement: Biochemical, biophysical, and potential physiological consequences, *Annu. Rev. Biophys.* **37**, 375 (2008).
- [6] G. Nettesheim, I. Nabti, C. U. Murade, G. R. Jaffe, S. J. King, and G. T. Shubeita, Macromolecular crowding acts as a physical regulator of intracellular transport, *Nat. Phys.* **16**, 1144 (2020).
- [7] A. F. Pegoraro, P. Janmey, and D. A. Weitz, Mechanical properties of the cytoskeleton and cells, *Cold Spring Harbor Perspect. Biol.* **9**, a022038 (2017).
- [8] M. D. Pierro, D. A. Potoyan, P. G. Wolynes, and J. N. Onuchic, Anomalous diffusion, spatial coherence, and viscoelasticity from the energy landscape of human chromosomes, *Proc. Natl. Acad. Sci. USA* **115**, 7753 (2018).
- [9] X. Fang and J. Wang, Nonequilibrium thermodynamics in cell biology: Extending equilibrium formalism to cover living systems, *Annu. Rev. Biophys.* **49**, 227 (2020).
- [10] A. A. Hyman and C. P. Brangwynne, Beyond stereospecificity: Liquids and mesoscale organization of cytoplasm, *Dev. Cell* **21**, 14 (2011).
- [11] K. A. Rosowski, T. Sai, E. Vidal-Henriquez, D. Zwicker, R. W. Style, and E. R. Dufresne, Elastic ripening and inhibition of liquid-liquid phase separation, *Nat. Phys.* **16**, 422 (2020).
- [12] S. Biswas, B. Mukherjee, and B. Chakrabarti, Thermodynamics predicts a stable microdroplet phase in polymer-gel mixtures undergoing elastic phase separation, *Soft Matter* **18**, 8117 (2022).
- [13] D. S. W. Lee, N. S. Wingreen, and C. P. Brangwynne, Chromatin mechanics dictates subdiffusion and coarsening dynamics of embedded condensates, *Nat. Phys.* **17**, 531 (2021).
- [14] Y. Zhang, D. S. W. Lee, Y. Meir, C. P. Brangwynne, and N. S. Wingreen, Mechanical frustration of phase separation in the cell nucleus by chromatin, *Phys. Rev. Lett.* **126**, 258102 (2021).
- [15] M. Heidenreich *et al.*, Designer protein assemblies with tunable phase diagrams in living cells, *Nat. Chem. Biol.* **16**, 939 (2020).

- [16] P. J. Flory, *Principles of Polymer Chemistry* (Cornell University Press, Ithaca, NY, 1953).
- [17] S. F. Banani, A. M. Rice, W. B. Peeples, Y. Lin, S. Jain, R. Parker, and M. K. Rosen, Compositional control of phase-separated cellular bodies, *Cell* **166**, 651 (2016).
- [18] T. S. Harmon, A. S. Holehouse, M. K. Rosen, and R. V. Pappu, Intrinsically disordered linkers determine the interplay between phase separation and gelation in multivalent proteins, *eLife* **6**, e30294 (2017).
- [19] P. Li *et al.*, Phase transitions in the assembly of multivalent signalling proteins, *Nature (London)* **483**, 336 (2012).
- [20] D. Bracha, M. T. Walls, M.-T. Wei, L. Zhu, M. Kurian, J. L. Avalos, J. E. Toettcher, and C. P. Brangwynne, Mapping local and global liquid phase behavior in living cells using photo-oligomerizable seeds, *Cell* **176**, 407 (2019).
- [21] Y. Shin, J. Berry, N. Pannucci, M. P. Haataja, J. E. Toettcher, and C. P. Brangwynne, Spatiotemporal control of intracellular phase transitions using light-activated optodroplets, *Cell* **168**, 159 (2017).
- [22] K. Murase, Y. Hirano, T.-P. Sun, and T. Hakoshima, Gibberellin-induced DELLA recognition by the gibberellin receptor GID1, *Nature (London)* **456**, 459 (2008).
- [23] T. Miyamoto, R. DeRose, A. Suarez, T. Ueno, M. Chen, T.-P. Sun, M. J. Wolfgang, C. Mukherjee, D. J. Meyers, and T. Inoue, Rapid and orthogonal logic gating with a gibberellin-induced dimerization system, *Nat. Chem. Biol.* **8**, 465 (2012).
- [24] M. L. L. Donnelly, G. Luke, A. Mehrotra, X. Li, L. E. Hughes, D. Gani, and M. D. Ryan, Analysis of the aphthovirus 2A/2B polyprotein “cleavage” mechanism indicates not a proteolytic reaction, but a novel translational effect: A putative ribosomal “skip”, *J. Gen. Virol.* **82**, 1013 (2001).
- [25] J. A. Anderson, C. D. Lorenz, and A. Travesset, General purpose molecular dynamics simulations fully implemented on graphics processing units, *J. Comput. Phys.* **227**, 5342 (2008).
- [26] J. A. Anderson, J. Glaser, and S. C. Glotzer, HOOMD-blue: A python package for high-performance molecular dynamics and hard particle Monte Carlo simulations, *Comput. Mater. Sci.* **173**, 109363 (2020).
- [27] G. Mitra, C. Chang, A. McMullen, D. Puchall, J. Brujic, and G. M. Hocky, A coarse-grained simulation model for colloidal self-assembly via explicit mobile binders, *Soft Matter* **19**, 4223 (2023).
- [28] J. A. Riback, C. D. Katanski, J. L. Kear-Scott, E. V. Pilipenko, A. E. Rojek, T. R. Sosnick, and D. A. Drummond, Stress-triggered phase separation is an adaptive, evolutionarily tuned response, *Cell* **168**, 1028 (2017).
- [29] D. S. W. Lee, C.-H. Choi, D. W. Sanders, L. Beckers, J. A. Riback, C. P. Brangwynne, and N. S. Wingreen, Size distributions of intracellular condensates reflect competition between coalescence and nucleation, *Nat. Phys.* **19**, 586 (2023).
- [30] J. L. Brewster, T. de Valoir, N. D. Dwyer, E. Winter, and M. C. Gustin, An osmosensing signal transduction pathway in yeast, *Science* **259**, 1760 (1993).
- [31] R. A. Saxton and D. M. Sabatini, mTOR signaling in growth, metabolism, and disease, *Cell* **169**, 361 (2017).
- [32] E. D. Siggia, Late stages of spinodal decomposition in binary mixtures, *Phys. Rev. A* **20**, 595 (1979).
- [33] I. M. Lifshitz and V. V. Slyozov, The kinetics of precipitation from supersaturated solid solutions, *J. Phys. Chem. Solids* **19**, 35 (1961).
- [34] P. Virtanen *et al.*, SciPy 1.0: Fundamental algorithms for scientific computing in python, *Nat. Methods* **17**, 261 (2020).
- [35] See Supplemental Material at <http://link.aps.org/supplemental/10.1103/PRXLife.2.033001> for cluster formation movies in MD simulations using HOOMD-blue comparing conditions with 0%, 30%, and 50% volume fractions of crowders over 22.4 s simulation time. Simulation renderings (top) with corresponding graph theory analyses (bottom) of cluster formation.
- [36] A. Zaccone and E. M. Terentjev, Theory of thermally activated ionization and dissociation of bound states, *Phys. Rev. Lett.* **108**, 038302 (2012).
- [37] B. R. Parry, I. V. Surovtsev, M. T. Cabeen, C. S. O’Hern, E. R. Dufresne, and C. Jacobs-Wagner, The bacterial cytoplasm has glass-like properties and is fluidized by metabolic activity, *Cell* **156**, 183 (2014).
- [38] Y. Xie, D. Gresham, and L. J. Holt, Increased mesoscale diffusivity in response to acute glucose starvation, *MicroPubl Biol* (2023), doi:10.17912/micropub.biology.000729.
- [39] P. Bursac, G. Lenormand, B. Fabry, M. Oliver, D. A. Weitz, V. Viasnoff, J. P. Butler, and J. J. Fredberg, Cytoskeletal remodelling and slow dynamics in the living cell, *Nat. Mater.* **4**, 557 (2005).
- [40] G. E. Peng, S. R. Wilson, and O. D. Weiner, A pharmacological cocktail for arresting actin dynamics in living cells, *Mol. Biol. Cell* **22**, 3986 (2011).
- [41] D. Loi, S. Mossa, and L. F. Cugliandolo, Effective temperature of active matter, *Phys. Rev. E* **77**, 051111 (2008).
- [42] C. M. Caragine, N. Kanellakopoulos, and A. Zidovska, Mechanical stress affects dynamics and rheology of the human genome, *Soft Matter* **18**, 107 (2021).
- [43] E. Moendarbary, L. Valon, M. Fritzsche, A. R. Harris, D. A. Moulding, A. J. Thrasher, E. Stride, L. Mahadevan, and G. T. Charras, The cytoplasm of living cells behaves as a poroelastic material, *Nat. Mater.* **12**, 253 (2013).
- [44] H. Turlier, D. A. Fedosov, B. Audoly, T. Auth, N. S. Gov, C. Sykes, J.-F. Joanny, G. Gompper, and T. Betz, Equilibrium physics breakdown reveals the active nature of red blood cell flickering, *Nat. Phys.* **12**, 513 (2016).
- [45] A. W. Harrison, D. A. Kenwright, T. A. Waigh, P. G. Woodman, and V. J. Allan, Modes of correlated angular motion in live cells across three distinct time scales, *Phys. Biol.* **10**, 036002 (2013).
- [46] S. C. Weber, M. A. Thompson, W. E. Moerner, A. J. Spakowitz, and J. A. Theriot, Analytical tools to distinguish the effects of localization error, confinement, and medium elasticity on the velocity autocorrelation function, *Biophys. J.* **102**, 2443 (2012).
- [47] C. P. Brangwynne, G. H. Koenderink, F. C. MacKintosh, and D. A. Weitz, Cytoplasmic diffusion: Molecular motors mix it up, *J. Cell Biol.* **183**, 583 (2008).
- [48] A. S. Lyon, W. B. Peeples, and M. K. Rosen, A framework for understanding the functions of biomolecular condensates across scales, *Nat. Rev. Mol. Cell Biol.* **22**, 215 (2021).
- [49] A. K. L. Leung, Poly(ADP-ribose): A dynamic trigger for biomolecular condensate formation, *Trends Cell Biol.* **30**, 370 (2020).
- [50] P. Yang *et al.*, G3BP1 is a tunable switch that triggers phase separation to assemble stress granules, *Cell* **181**, 325 (2020).
- [51] Y. Lin, D. S. W. Protter, M. K. Rosen, and R. Parker, Formation and maturation of phase-separated liquid droplets by RNA-binding proteins, *Mol. Cell* **60**, 208 (2015).

- [52] L. Deng, X. Trepap, J. P. Butler, E. Millet, K. G. Morgan, D. A. Weitz, and J. J. Fredberg, Fast and slow dynamics of the cytoskeleton, *Nat. Mater.* **5**, 636 (2006).
- [53] M. Guo, A. J. Ehrlicher, M. H. Jensen, M. Renz, J. R. Moore, R. D. Goldman, J. Lippincott-Schwartz, F. C. Mackintosh, and D. A. Weitz, Probing the stochastic, motor-driven properties of the cytoplasm using force spectrum microscopy, *Cell* **158**, 822 (2014).
- [54] A. Patel, L. Malinowska, S. Saha, J. Wang, S. Alberti, Y. Krishnan, and A. A. Hyman, ATP as a biological hydrotrope, *Science* **356**, 753 (2017).
- [55] D. Zwicker, R. Seyboldt, C. A. Weber, A. A. Hyman, and F. Jülicher, Growth and division of active droplets provides a model for protocells, *Nat. Phys.* **13**, 408 (2016).
- [56] B. Guillas *et al.*, ATP-driven separation of liquid phase condensates in bacteria, *Mol. Cell* **79**, 293 (2020).
- [57] S. Saurabh, T. N. Chong, C. Bayas, P. D. Dahlberg, H. N. Cartwright, W. E. Moerner, and L. Shapiro, ATP-responsive biomolecular condensates tune bacterial kinase signaling, *Sci. Adv.* **8**, eabm6570 (2022).
- [58] R. M. Garner, A. T. Molines, J. A. Theriot, and F. Chang, Vast heterogeneity in cytoplasmic diffusion rates revealed by Nanorheology and Doppelgänger simulations, *Biophys. J.* **122**, 767 (2023).
- [59] D. Sang, T. Shu, C. F. Pantoja, A. Ibáñez de Opakua, M. Zweckstetter, and L. J. Holt, Condensed-phase signaling can expand kinase specificity and respond to macromolecular crowding, *Mol. Cell* **82**, 3693 (2022).
- [60] D. C. Amberg, D. J. Burke, and J. N. Strathern, High-efficiency transformation of yeast, *Cold Spring Harbor Protoc.* **2006**, pdb.prot4145 (2006).
- [61] M. C. Munder *et al.*, A pH-driven transition of the cytoplasm from a fluid- to a solid-like state promotes entry into dormancy, *eLife* **5**, e09347 (2016).
- [62] A. Zidovska, D. A. Weitz, and T. J. Mitchison, Micron-scale coherence in interphase chromatin dynamics, *Proc. Natl. Acad. Sci. USA* **110**, 15555 (2013).
- [63] J.-Y. Tinevez, N. Perry, J. Schindelin, G. M. Hoopes, G. D. Reynolds, E. Laplantine, S. Y. Bednarek, S. L. Shorte, and K. W. Eliceiri, TrackMate: An open and extensible platform for single-particle tracking, *Methods* **115**, 80 (2017).
- [64] J. Schindelin *et al.*, Fiji: an open-source platform for biological-image analysis, *Nat. Methods* **9**, 676 (2012).
- [65] J. Schindelin, C. T. Rueden, M. C. Hiner, and K. W. Eliceiri, The ImageJ ecosystem: An open platform for biomedical image analysis, *Mol. Reprod. Dev.* **82**, 518 (2015).
- [66] A. X. Lu, T. Zarin, I. S. Hsu, and A. M. Moses, YeastSpotter: accurate and parameter-free web segmentation for microscopy images of yeast cells, *Bioinformatics* **35**, 4525 (2019).
- [67] A. Shivanandan, A. Radenovic, and I. F. Sbalzarini, MosaicIA: An ImageJ/Fiji plugin for spatial pattern and interaction analysis, *BMC Bioinf.* **14**, 349 (2013).
- [68] F. Etoc, E. Balloul, C. Vicario, D. Normanno, D. Liße, A. Sittner, J. Piehler, M. Dahan, and M. Coppey, Publisher correction: Non-specific interactions govern cytosolic diffusion of nanosized objects in mammalian cells, *Nat. Mater.* **17**, 1048 (2018).
- [69] G. Csárdi and T. Nepusz, The igraph software package for complex network research, *InterJ. Complex Syst.* **1695**, 1 (2006).
- [70] A. H. Larsen and T. Nepusz, The atomic simulation environment—a python library for working with atoms, *J. Phys. Condens. Matter* **29**, 273002 (2017).
- [71] S. Thomas, M. Alberts, M. M. Henry, C. E. Estridge, and E. Jankowski, Routine million-particle simulations of epoxy curing with dissipative particle dynamics, *J. Theor. Comput. Chem.* **17**, 1840005 (2018).
- [72] N. Metropolis and S. Ulam, The Monte Carlo method, *J. Am. Stat. Assoc.* **44**, 335 (1949).
- [73] O. Maxian, A. Donev, and A. Mogilner, Interplay between Brownian motion and cross-linking controls bundling dynamics in actin networks, *Biophys. J.* **121**, 1230 (2022).
- [74] S. Marbach and C. E. Miles, Coarse-grained dynamics of transiently-bound fast linkers, *J. Chem. Phys.* **158**, 214117 (2023).
- [75] M. P. Howard, J. A. Anderson, A. Nikoubashman, S. C. Glotzer, and A. Z. Panagiotopoulos, Efficient neighbor list calculation for molecular simulation of colloidal systems using graphics processing units, *Comput. Phys. Commun.* **203**, 45 (2016).
- [76] L. S. Tee, S. Gotoh, and W. E. Stewart, Molecular parameters for normal fluids. Lennard-Jones 12–6 potential, *Ind. Eng. Chem. Fundam.* **5**, 356 (1966).
- [77] J.-P. Hansen and L. Verlet, Phase transitions of the Lennard-Jones system, *Phys. Rev.* **184**, 151 (1969).
- [78] J. J. Nicolas, K. E. Gubbins, W. B. Streett, and D. J. Tildesley, Equation of state for the Lennard-Jones fluid, *Mol. Phys.* **37**, 1429 (1979).
- [79] B. Smit, Phase diagrams of Lennard-Jones fluids, *J. Chem. Phys.* **96**, 8639 (1992).
- [80] C. L. Phillips, J. A. Anderson, and S. C. Glotzer, Pseudo-random number generation for Brownian dynamics and dissipative particle dynamics simulations on GPU devices, *J. Comput. Phys.* **230**, 7191 (2011).
- [81] J. B. Alberts and G. M. Odell, In silico reconstitution of listeria propulsion exhibits nano-saltation, *PLoS Biol.* **2**, e412 (2004).